



UNIVERSITÀ  
POLITECNICA  
DELLE MARCHE

FACULTY OF ENGINEERING

Master's degree in Biomedical Engineering

---

**Finite-Difference Time-Domain Analysis of  
Time Reversal Technique for Electromagnetic  
Fields Focusing on Human Head**

Advisor:

*Prof. Franco Moglie*

Candidate:

Francesco Dragano

---

Academic Year 2020-2021



# I. Contents

<b>1. Introduction</b>	<b>1</b>
<b>1.1 Finite Difference Time Domain Method</b>	<b>1</b>
1.1.1 Historical Background	2
1.1.2 Working Principle	2
1.1.3 Boundary Condition	10
1.1.4 Advantages and Disadvantages of FDTD modelling	11
<b>1.2 Time Reversal</b>	<b>13</b>
1.2.1 Historical Background and Applications	14
1.2.2 Working Principle	15
1.2.3 Electromagnetic Time Reversal	16
1.2.4 Electromagnetic Time Reversal in Reverberation Chamber	20
1.2.5 Time Reversal in a Linear Time Invariant System	25
<b>1.3 Dielectric Properties of Body Tissue</b>	<b>29</b>
1.3.1 Dielectric theory	30
1.3.2 Application in Human Tissue	31
1.3.3 Cole-Cole Equation	34
<b>2. Thesis Aim</b>	<b>36</b>
<b>3. Materials and Methods</b>	<b>37</b>
3.1 Numerical Human Model	37
3.2 FDTD Modelling of TR	41
3.3 Permittivity Value Extraction	44
<b>4. Results and Discussion</b>	<b>48</b>
<b>5. Conclusions</b>	<b>62</b>
<b>6. Bibliography</b>	<b>64</b>

## II. Tables' list

Table 1 Human tissues and their densities. _____	45
Table 2 Parameters to assess to compute the complex dielectric constant for body tissues _____	46
Table 3 Dielectric constant and conductivity for studied human tissues. _____	47

### III. Figures' List

Figure 1 The Yee lattice schematic representation as a single cubic voxel with dimension  $\Delta x \times \Delta y \times \Delta z$ . The three components of electric field are placed on the edges of the cube in the corresponding direction, instead the three magnetic field components are stored on the cube faces. \_\_\_\_\_ 6

Figure 2 Yee's one-dimensional scheme for updating electromagnetic field in space and time. \_\_\_\_\_ 7

Figure 3 Finite-Difference Time-Domain algorithm flowchart. \_\_\_\_\_ 9

Figure 4 Representation of Perfect Matching Layer in truncate 2D computational domain. \_\_\_\_\_ 11

Figure 5 Photograph of ripples propagating outward from the location at which pebble enters the water. \_\_\_\_\_ 13

Figure 6 Electromagnetic Time Reversal process with a time reversal cavity: forward propagation and measurement (a), time reversing and back-propagation (b). \_\_\_\_\_ 17

Figure 7 Electromagnetic Time Reversal process with a time reversal mirror: forward propagation and measurement (a), time reversing and back-propagation. \_\_\_\_\_ 18

Figure 8 Electromagnetic Time Reversal forward propagation detection with a unique probe in reverberation chamber. \_\_\_\_\_ 18

Figure 9 Reverberation chamber at Otto-von-Guericke-University Magdeburg, Germany. On the left side the vertical stirrer mode is placed, ensuring a statistically homogeneous field distribution. \_\_\_\_\_ 21

Figure 10 Modes in a rectangular cavity resonator. The goal is to excite as more modes as possible, so that the field within the chamber is a combination of maximums and minimums which tend to be chaotic. Excitable modes enhance with the frequency. \_\_\_\_\_ 22

Figure 11 Scheme of electromagnetic time reversal in reverberation chamber: (a) excitation pulse; (b) received signal; (c) reversed received signal; (d) time focusing; (e) space focusing. \_\_\_\_\_ 23

Figure 12 . Linear time-invariant system. \_\_\_\_\_ 25

Figure 13 Linear time-invariant system after Time Reversal application. \_\_\_\_\_ 28

Figure 14 Dielectric polarization verified when a dielectric material is placed in an electric field. \_\_\_\_\_ 30

Figure 15 Logarithmic trend of the typical frequency variation of dielectric permittivity real part for a typical biological tissue. \_\_\_\_\_ 33

Figure 16 The Virtual Family models. From left to right: Duke, Ella; Billie, Thelonious. \_\_\_\_\_ 38

Figure 17 Detailed representation of Thelonious. From left to right: skin, muscle, inner organs, blood vessels and skeleton. \_\_\_\_\_ 38

Figure 18 Duke's head representation. From left to right: skin, skull, brain, and white matter. \_\_\_\_\_ 39

Figure 19 Frontal plane view of Thelonious' model in ParaView software. \_\_\_\_\_ 40

Figure 20 Sagittal plane view of Thelonious' reduced model in ParaView software. \_\_\_\_\_ 40

Figure 21 Scheme of second phase of electromagnetic time reversal in reflecting environment: once recorded the signal on the target point (in the head), it is time reversed and rebroadcasted from monopole to target point. _____	42
Figure 22 Comparison between the original input gaussian pulse signal centered at 2.45 GHz (with a bandwidth of 300 MHz) and the received signal on the target point (Simulation I). Both signals are normalized to their maximum values. _____	49
Figure 23 Original signal vs reconstructed signal (Simulation I). _____	49
Figure 24 Original signal overlapped to the reconstructed signal (Simulation I). _____	50
Figure 25 Original vs received signal (Simulation II). _____	51
Figure 26 Cartesian components of received signal at target point (Simulation II). _____	51
Figure 27 Original signal vs reconstructed signal (Simulation II). _____	52
Figure 28 Original signal overlapped to the reconstructed signal (Simulation II). _____	52
Figure 29 Original vs received signal (Simulation III). _____	54
Figure 30 Original signal vs reconstructed signal (Simulation III). _____	54
Figure 31 Original signal overlapped to the reconstructed signal (Simulation III). _____	55
Figure 32 Original vs received signal (Simulation IV). _____	56
Figure 33 Original signal vs reconstructed signal (Simulation IV). _____	56
Figure 34 Original signal overlapped to the reconstructed signal (Simulation IV). _____	57
Figure 35 Contour plot of electromagnetic fields related to the transmission of the original input signal to the target point (Simulation IV). _____	58
Figure 36 Contour plot of electromagnetic field after the application of TR (Simulation IV). _____	58
Figure 37 Contour plot of electromagnetic fields related to the transmission of the original input signal to the target point (Simulation I). _____	59
Figure 38 Contour plot of electromagnetic fields related to the transmission of the original input signal to the target point (Simulation II). _____	59
Figure 39 Contour plot of electromagnetic field after the application of TR (Simulation I). At the top there is a frame earlier than the one at the bottom. _____	60
Figure 40 Contour plot of electromagnetic field after the application of TR (Simulation II). At the top there is a frame earlier than the one at the bottom. _____	61

## IV. Abstract

The interaction between electromagnetic fields and human body has been studied for a long time, accounting for one of the most operative areas in theoretical and applied research concerning with the technologies of electromagnetism. Initially, the studies of the scientific community were focused on the possible harmful effects of the interaction between electromagnetic fields and the human body, forming a branch of physics named as radiation dosimetry. For some years now, the innovative idea of using this phenomenon to produce a specific effect has been taken into consideration. This innovation has met with great success in medical branch thanks to the nature of non-ionizing electromagnetic fields, their ability to penetrate matter, and the specificity of the electromagnetic properties of the different human tissues, also according to the several pathological conditions. Consequently, some diagnostic and therapeutic technologies have been introduced into clinical routine. Some examples are the Magnetic Resonance Imaging and the Tomographic Microwave Imaging for diagnostic applications and Microwave-induced hyperthermia and Radar therapy for the treatment of some diseases. Other methodologies are being developed to cooperate with those currently in use to enhance the quality of the diagnosis or the therapeutic efficacy for certain diseases. New approaches to overcome the limitations of current methodologies are based on the usage of the Time Reversal (TR) technique. Recently applied on electromagnetism, the TR exploits the principle of reciprocity to focus wave energy to a selected point in space and time. In the present thesis, we propose a numerical study of TR principles to focus, both spatially and temporally, electromagnetic fields on human head. The computation is done by own-made Finite-Difference Time-Domain (FDTD) code, capable to account for tissues permittivity. A human numerical model from the Virtual Family project is used and permittivity values are assigned to each tissue according to Cole-Cole equation. A gaussian pulse is broadcasted by a monopole antenna, spread out by reverberation chamber, and measured, by FDTD code, on a point in the head in which we desire to focus energy.

The FDTD-computed signal is then time reversed and rebroadcasted to target tissue. Promising results are obtained. This thesis extends the previous works, by introducing FDTD simulations of a finer map of human body on high-performance computers, enhancing the design of applicators based on TR technique, to focus energy on the target tissue, while minimizing the side effects on the surrounding ones.





# 1. Introduction

This section provides a theoretical background about the concepts underlying the present study. The sequel of this section begins with the description of Finite-Difference Time-Domain method. Then, basic principles of Time Reversal (TR) technique are discussed. Finally, dielectric properties of body tissues are outlined.

## 1.1 Finite Difference Time Domain Method

In this chapter the fundamentals of the FDTD method to solve Maxwell's equations in the time domain are given in a concise form together with advantages and weakness. FDTD or Yee's (after K.S. Yee) method is a numerical process used for modelling the electromagnetic field interaction between physical objects with complex geometries and the environment [1]. Being a time-domain method, FDTD solutions comprise a broad range of frequencies through a single simulation run and allow to handle non-linear material in a natural manner. FDTD is a finite difference method, thus it belongs in the general class of grid-based differential numerical modelling methods. It is based on the discretization of the time-dependent Maxwell's equations, both in the space and in the time, respectively through central-difference approximations and partial derivatives. The resulting differential equations are numerically solved. Given a certain time instant, the components of the electric field vector in a three-dimensional (3D) space are determined and the components of the magnetic field of the same 3D space are solved at the next time instant. The process is iteratively repeated until the target electromagnetic field is completely represented [2]. Nowadays, FDTD represents one of the most popular techniques for the solution of electromagnetic problems, principally due to its relative simplicity both in basic concept and in computer implantation. Examples of systems that can be modelled by FDTD are: antennas, humans, aircrafts, satellites, and meta-materials.

### ***1.1.1 Historical Background***

The classical finite difference schemes for solving second-order wave equation in one-dimensional (1-D), two-dimensional (2-D) or three-dimensional (3D) space together with the finding of conditional stability of explicit time-dependent finite difference schemes were published in 1928, by Courant, Friedrichs and Lewy [3]. This discovery has found a wide application in computational fluid dynamics problems for several years [4]. In 1966, the Chinese American electrical engineer and mathematician Kane Shee-Gong Yee published a paper on the usage of finite difference staggered grids algorithm to solve the Maxwell's equations [5]. Yee's pioneering finding was the application of centered finite difference operators on staggered grids in space and time for each electric and magnetic vector field component in Maxwell's curl equations. The heading "Finite-difference Time-Domain" and its relative acronym "FDTD" were proposed by Taflove in 1980 [6]. During the past 25 years the FDTD method has become the most spread applied simulation tool among scientific and engineering problems dealing with electromagnetic phenomena [1]. Contemporary applications of FDTD mainly concern with the modelling of microwaves for radar technology, antennas, biomedical treatment/imaging.

### ***1.1.2 Working Principle***

FDTD is a discrete approximation of Maxwell's equations that numerically and concomitantly solve in both time and space. It calculates the magnetic and electric fields as a function of time (starting at  $t=0$ ) and everywhere in the computational domain. Let consider an isotropic, time-invariant and homogeneous medium [1]. The time-domain electromagnetic is described by two Maxwell's curl equations:

$$\nabla \times \mathbf{E} = -\frac{\partial \mathbf{B}}{\partial t} - \mathbf{M} \quad (1)$$

$$\nabla \times \mathbf{H} = \frac{\partial \mathbf{D}}{\partial t} + \mathbf{J} \quad (2)$$

Where  $\mathbf{E}$  and  $\mathbf{H}$  are respectively the electric and magnetic fields,  $\mathbf{D}$  and  $\mathbf{B}$  are respectively the electric and magnetic flux densities and  $\mathbf{J}$  and  $\mathbf{M}$  are respectively the volume electric and magnetic current densities [1]. The following relationships hold:

$$\mathbf{D} = \varepsilon \mathbf{E} \quad (3)$$

$$\mathbf{B} = \mu \mathbf{H} \quad (4)$$

$$\mathbf{J} = \sigma \mathbf{E} \quad (5)$$

$$\mathbf{M} = \sigma_m \mathbf{H} \quad (6)$$

Where  $\varepsilon$  is the permittivity,  $\mu$  is the permeability,  $\sigma$  is the electric conductivity and  $\sigma_m$  is the magnetic conductivity of the medium [1]. Considering a medium without any electric or magnetic loss, (1) and (2) can be rewritten as follow:

$$\frac{\partial \mathbf{H}}{\partial t} = -\frac{1}{\mu} \nabla \times \mathbf{E} \quad (7)$$

$$\frac{\partial \mathbf{E}}{\partial t} = -\frac{1}{\varepsilon} \nabla \times \mathbf{H} \quad (8)$$

Decomposing along x, y and z axis both electrical and magnetic field, it is possible to write six scalar equations (one for each field component) in the Cartesian coordinate system [1]:

$$\frac{\partial E_x}{\partial t} = \frac{1}{\varepsilon} \left( \frac{\partial H_z}{\partial y} - \frac{\partial H_y}{\partial z} - \sigma E_x \right) \quad (9)$$

$$\frac{\partial E_y}{\partial t} = \frac{1}{\varepsilon} \left( \frac{\partial H_x}{\partial z} - \frac{\partial H_z}{\partial x} - \sigma E_y \right) \quad (10)$$

$$\frac{\partial E_z}{\partial t} = \frac{1}{\varepsilon} \left( \frac{\partial H_y}{\partial x} - \frac{\partial H_x}{\partial y} - \sigma E_z \right) \quad (11)$$

$$\frac{\partial H_x}{\partial t} = \frac{1}{\mu} \left( \frac{\partial E_y}{\partial z} - \frac{\partial E_z}{\partial y} \right) \quad (12)$$

$$\frac{\partial H_y}{\partial t} = \frac{1}{\mu} \left( \frac{\partial E_z}{\partial x} - \frac{\partial E_x}{\partial z} \right) \quad (13)$$

$$\frac{\partial H_z}{\partial t} = \frac{1}{\mu} \left( \frac{\partial E_x}{\partial y} - \frac{\partial E_y}{\partial x} \right) \quad (14)$$

Then it is required to implement the six scalar partial derivative equations in a computer in order to solve them and thus to point out the interaction of electromagnetic waves with object under study [1]. Therefore, it is required a space-time discretization: FDTD divides a space point into box-shaped cells and assesses the electromagnetic field in that discrete point in a certain time instant [1].

$$(i, j, k) = (i\Delta x, j\Delta y, k\Delta z) \quad (15)$$

Where  $\Delta x$ ,  $\Delta y$  and  $\Delta z$  are the cell space increments in the  $x$ ,  $y$  and  $z$  coordinate directions respectively and  $i$ ,  $j$  and  $k$  are integers. Denoting by  $F$  any scalar function of space and time evaluated at a discrete point in the grid and at a discrete point in time:

$$F_{i,j,k}^n = (i\Delta x, j\Delta y, k\Delta z, n\Delta t) \quad (16)$$

Using central, finite difference approximation in space:

$$\frac{\partial F}{\partial x}(i\Delta x, j\Delta y, k\Delta z, n\Delta t) = \frac{F_{i+\frac{1}{2},j,k}^n - F_{i-\frac{1}{2},j,k}^n}{\Delta x} + O((\Delta x)^2) \quad (17)$$

$$\frac{\partial F}{\partial y}(i\Delta x, j\Delta y, k\Delta z, n\Delta t) = \frac{F_{i,j+\frac{1}{2},k}^n - F_{i,j-\frac{1}{2},k}^n}{\Delta y} + O((\Delta y)^2) \quad (18)$$

$$\frac{\partial F}{\partial z}(i\Delta x, j\Delta y, k\Delta z, n\Delta t) = \frac{F_{i,j,k+\frac{1}{2}}^n - F_{i,j,k-\frac{1}{2}}^n}{\Delta z} + O((\Delta z)^2) \quad (19)$$

Using central, finite difference approximation in time:

$$\frac{\partial F}{\partial t}(i\Delta x, j\Delta y, k\Delta z, n\Delta t) = \frac{F_{i,j,k}^{n+\frac{1}{2}} - F_{i,j,k}^{n-\frac{1}{2}}}{\Delta t} + O((\Delta t)^2) \quad (20)$$

Note that the discretization both in space and time is obtained following the definition of the first order derivative of the scalar function, therefore there is also an error (which depends on the square of the distance or of the time), cause of solutions uncertainty [1]. Considering the electrical losses, scalar equations are discretized as:

$$E_{x(i,j,k)}^{n+1} = \left(\frac{2\varepsilon - \sigma\Delta t}{2\varepsilon + \sigma\Delta t}\right) E_{x(i,j,k)}^n + \frac{2\Delta t}{\Delta y(2\varepsilon + \sigma\Delta t)} \left(H_{z(i,j,k+1)}^{n+\frac{1}{2}} - H_{z(i,j,k)}^{n+\frac{1}{2}}\right) - \frac{2\Delta t}{\Delta z(2\varepsilon + \sigma\Delta t)} \left(H_{z(i,j,k+1)}^{n+\frac{1}{2}} - H_{z(i,j,k)}^{n+\frac{1}{2}}\right) \quad (21)$$

$$E_{y(i,j,k)}^{n+1} = \left(\frac{2\varepsilon - \sigma\Delta t}{2\varepsilon + \sigma\Delta t}\right) E_{y(i,j,k)}^n + \frac{2\Delta t}{\Delta z(2\varepsilon + \sigma\Delta t)} \left(H_{z(i,j,k+1)}^{n+\frac{1}{2}} - H_{z(i,j,k)}^{n+\frac{1}{2}}\right) - \frac{2\Delta t}{\Delta x(2\varepsilon + \sigma\Delta t)} \left(H_{z(i+1,j,k)}^{n+\frac{1}{2}} - H_{z(i,j,k)}^{n+\frac{1}{2}}\right) \quad (22)$$

$$E_{z(i,j,k)}^{n+1} = \left(\frac{2\varepsilon - \sigma\Delta t}{2\varepsilon + \sigma\Delta t}\right) E_{z(i,j,k)}^n + \frac{2\Delta t}{\Delta x(2\varepsilon + \sigma\Delta t)} \left(H_{z(i+1,j,k)}^{n+\frac{1}{2}} - H_{z(i,j,k)}^{n+\frac{1}{2}}\right) - \frac{2\Delta t}{\Delta y(2\varepsilon + \sigma\Delta t)} \left(H_{z(i,j,k+1)}^{n+\frac{1}{2}} - H_{z(i,j,k)}^{n+\frac{1}{2}}\right) \quad (23)$$

$$H_{x(i,j,k)}^{n+\frac{1}{2}} = H_{x(i,j,k)}^{n-\frac{1}{2}} + \frac{\Delta t}{\mu\Delta z} (E_{y(i,j,k)}^n - E_{y(i,j,k-1)}^n) - \frac{\Delta t}{\mu\Delta y} (E_{z(i,j,k)}^n - E_{z(i,j-1,k)}^n) \quad (24)$$

$$H_{y(i,j,k)}^{n+\frac{1}{2}} = H_{y(i,j,k)}^{n-\frac{1}{2}} + \frac{\Delta t}{\mu\Delta x} (E_{z(i,j,k)}^n - E_{z(i-1,j,k)}^n) - \frac{\Delta t}{\mu\Delta z} (E_{z(i,j,k)}^n - E_{z(i,j,k-1)}^n) \quad (25)$$

$$H_{z(i,j,k)}^{n+\frac{1}{2}} = H_{z(i,j,k)}^{n-\frac{1}{2}} + \frac{\Delta t}{\mu\Delta y}(E_{y(i,j,k)}^n - E_{y(i,j-1,k)}^n) - \frac{\Delta t}{\mu\Delta x}(E_{z(i,j,k)}^n - E_{z(i-1,j,k)}^n) \quad (26)$$

The Yee algorithm places the vector components of E and H about rectangular unit cells of a Cartesian computational grid so that each E component is surrounded by four circulating H components, and conversely [5]. This scheme is named as Yee lattice and is shown in Figure 1. The domain becomes an interconnected array of Faraday's and Ampere's laws at the boundary. To map an electromagnetic wave interaction structure into the Yee lattice, it is required to set appropriate values of permittivity and permeability to each component of E and H, respectively [5].

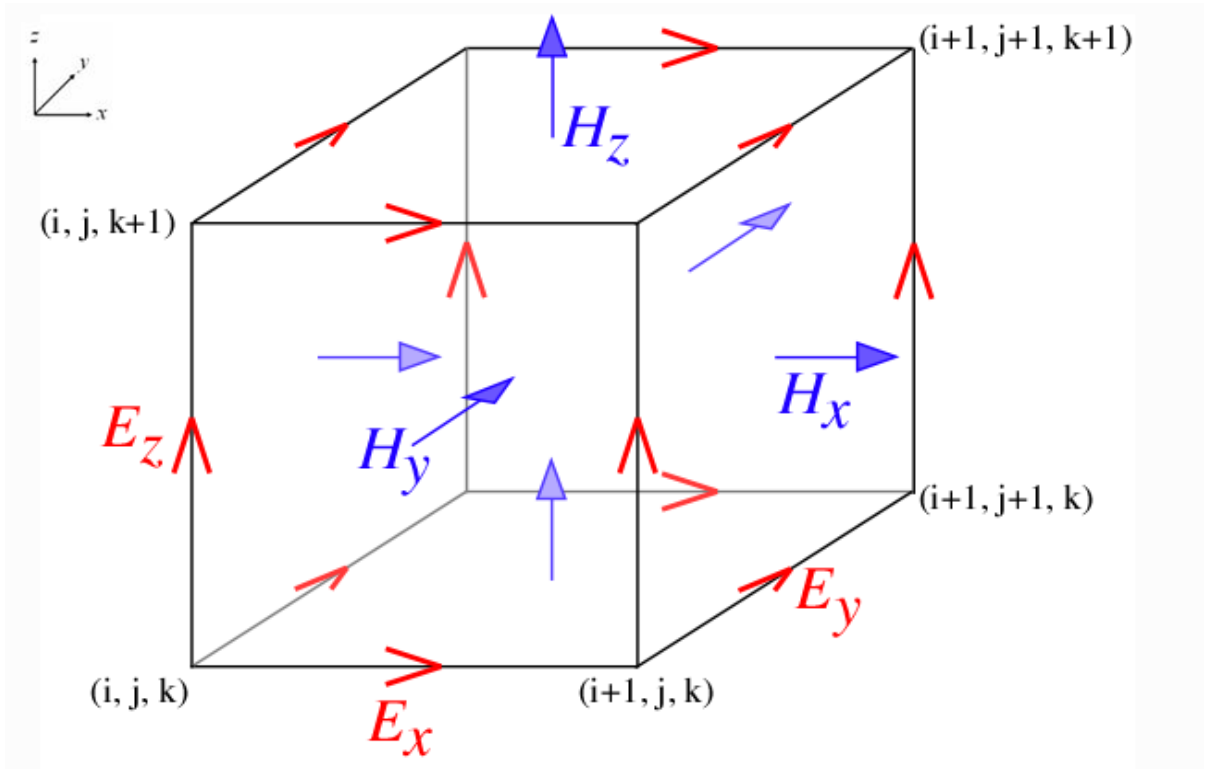


Figure 1 The Yee lattice schematic representation as a single cubic voxel with dimension  $\Delta x \times \Delta y \times \Delta z$ . The three components of electric field are placed on the edges of the cube in the corresponding direction, instead the three magnetic field components are stored on the cube faces.

Besides, Yee proposed a “leap-frog” algorithm: to solve Maxwell’s equation in space and time, one should compute first all  $\mathbf{H}$  vector components, then all  $\mathbf{E}$  vector components remembering that  $\mathbf{E}$  and  $\mathbf{H}$  field components are shifted by half of the discretization  $\Delta x$  in time, as schematically shown in Figure 2 [5]. In summary, at any point in space, the updated value of  $\mathbf{E}$  in time depends on both stored value of  $\mathbf{E}$  and numerical curl of local distribution of  $\mathbf{H}$  in the space. Reversely, at each point in space, the updated value of the  $\mathbf{H}$  in time depends on both stored value of  $\mathbf{H}$  and numerical curl of local distribution of  $\mathbf{E}$  in the space. Iterating the update process will result in a time propagation of electromagnetic waves under investigation in a numerical grid stored into computer RAM.

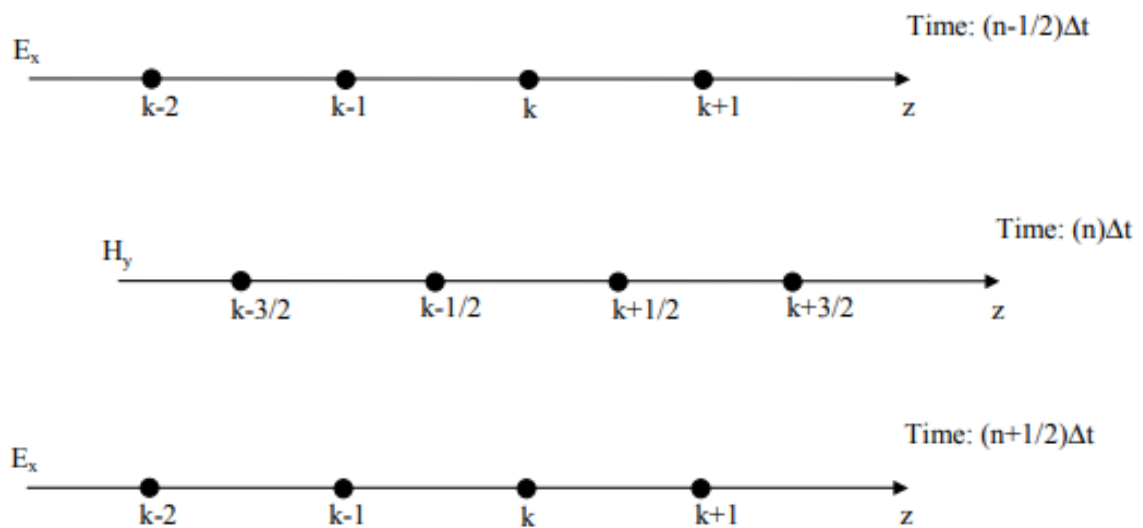


Figure 2 Yee's one-dimensional scheme for updating electromagnetic field in space and time.

To implement the FDTD algorithm is necessary to firstly define the computational domain, which is the physical region over which the simulation will work. Also, material (either metal, dielectric, or free-space) of each cell within the computational domain must be assigned by setting permeability, permittivity, and conductivity parameters. Then the source is specified, generally as current on a wire, applied electric field or impinging plane wave.



The output is the time evolution of  $\mathbf{E}$  and  $\mathbf{H}$  for each point in the computational domain. Data processing can occur during the ongoing simulation. Moreover, stability conditions must be respected. Since the algorithm requires discretization in both time and space and so functions of a continuous variable are represented in the computer by a finite number of evaluations, it results a discretization error. To minimize this error, stability conditions must be respected both in space and time. First, the cell must be little enough to describe the complex geometry of the structure and simultaneously big enough with respect to the smallest wavelength in the simulation. Considering square cells ( $\Delta x = \Delta y = \Delta z = \Delta$ ):

$$\Delta \leq \frac{\lambda_{min}}{10} \quad (27)$$

$$\Delta = \frac{\lambda_{min}}{20} \quad (28)$$

It has been verified that at least ten cells per wavelength are required to obtain a meaningful representation, having an error of about 10% [7]. The best case is (28) with an error of about 1%. If dielectrics are considered in the simulation, it must be firstly computed the wavelength in the dielectric with higher dielectric constant and losses and then consider the cell size at least ten time smaller than that value [7]. Also, the Courant-Friedrichs-Lewy condition must be satisfied to ensure the convergence of the system [7], that for uniform grid with equal cell dimensions is:

$$\Delta t \leq \frac{\Delta}{c_0 \sqrt{d}} \quad (29)$$

Where  $\Delta t$  is the time-step,  $\Delta$  is the smallest cell size (in 3D,  $\Delta = \Delta x = \Delta y = \Delta z$ ),  $c_0$  is the wave propagation at the speed of light and  $d = 1, 2$  or  $3$  for one-, two- or three-dimensional problem respectively [7].

To respect the stability condition, the propagation of a field component cannot be higher than one cell size in the time-step  $\Delta t$  [7]. To increase the mesh resolution, smaller time-step need to be used, which will require a larger number of time-steps to achieve the convergence. The flowchart of FDTD algorithm is reported in Figure 3.

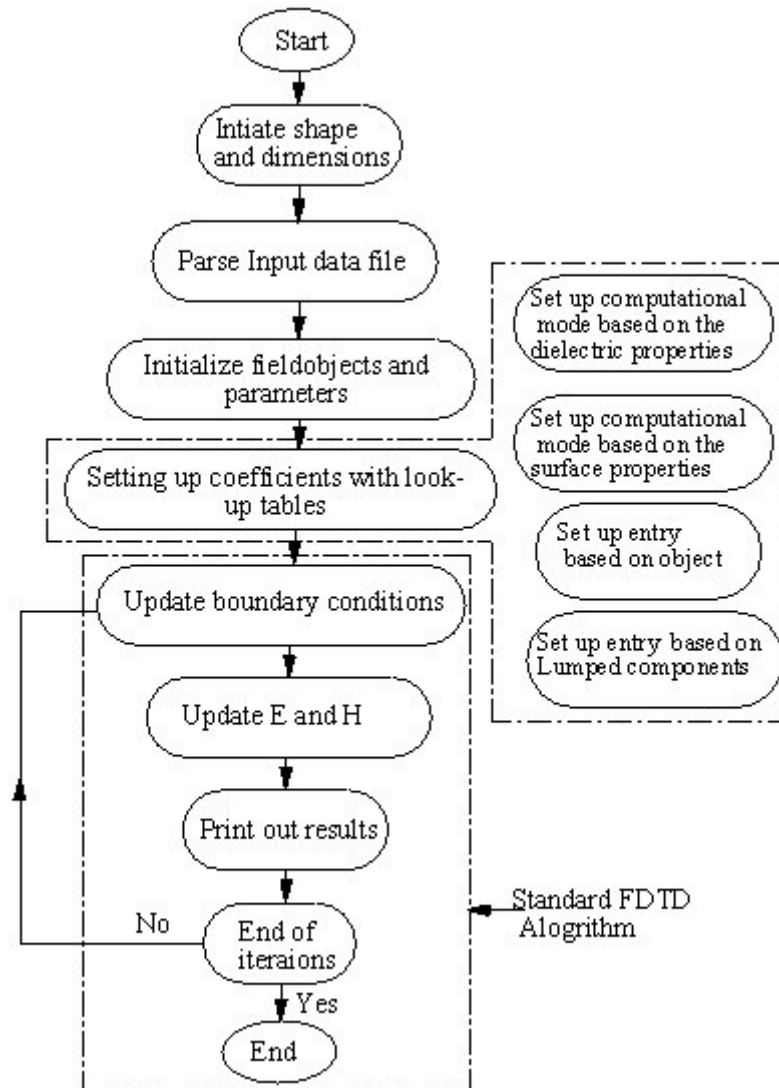


Figure 3 Finite-Difference Time-Domain algorithm flowchart.

### ***1.1.3 Boundary Condition***

FDTD algorithm directly determines the electromagnetic fields in all the points of computational domain. It must be a finite space since there are no processors with unlimited amount of storage space. The problem is irrelevant when simulating spatially limited structure (i.e., a waveguide or a resonator) where the aim is to model a region that “capture” the field inside [7]. In the majority of cases, it is required to simulate open space regions and to limit the FDTD grid are used Absorbing Boundary Conditions (ABCs), also named as Radiation Boundary Conditions (RBCs) [7]. In literature, several ABCs have been proposed resorting either to analytical approximations of the wave equation or to the usage of fictive absorbing materials to physically absorb the outgoing wave, theoretically without any back reflection [7]. One common ABC is that proposed by G. Mur in 1981 [8]. It allows to compute the boundary field values from the three-dimensional scalar wave equations. Mur’s ABC has easy implementation, especially in case of plane waves propagation perpendicular to the space inside the imposed limits, but it causes a consistent error due to not negligible wave reflections. In 1994, J.P. Berenger introduced the Perfectly Matching Layer (PML) concept [9], which has undergone several changes and extensions in the following years. Technically the PML is an absorbing region rather than a boundary condition per se and it is capable to absorb all the outgoing waves propagating toward the boundaries [9]. Instead of the usage of simple surrounding boundary, it is based on the usage of layers of cells enclosing the computational domain. These layers have to satisfy two conditions. First, the wave impedance inside the layer should be equal to that of the computational domain being truncated; the name PML derives from this concept [9] [10]. Second, the PML should have losses so that incoming electromagnetic wave is gradually damped while travelling through it [9] [10].

In detail, PML is designed so that an artificial conductivity is inserted in such way that it begins with very small values (zero losses) in the computational domain-PML interfaces and subsequently grows until it reaches its maximum value in the last PML layer [9] [10]. Consequently, the amplitude of incoming electromagnetic fields goes from a maximum value at the computational domain-PML interfaces to zero in the last PML layer, following an exponential decay [9] [10]. Generally, the last layer is a Perfect Electrical Conductor (PEC). The standard Berenger PML consists of different PML layers: left and right x-oriented PMLs, top and bottom y-oriented PMLs, and four corner xy-oriented PMLs, as illustrated in Figure 4 [10]. PML implementation is more computation- and time-expanding, but it can provide orders-of-magnitude lower reflections with respect to Mur's ABS, thus it is generally preferred.

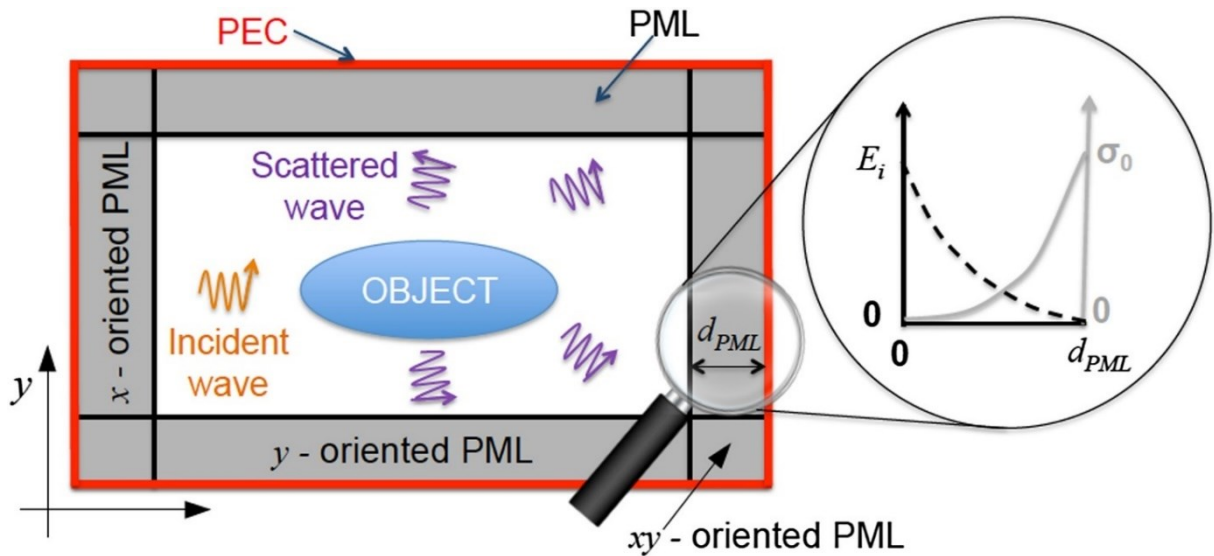


Figure 4 Representation of Perfect Matching Layer in truncate 2D computational domain.

### 1.1.4 Advantages and Disadvantages of FDTD modelling

The following advantages make the FDTD method widely spread:

- Accurate, robust, and systematic method [11].
- Applicable to materials with any conductivity [11].

- Easy to understand and develop (simple parametrization and implementation), so users can easily understand how to use it and know what to expect from the modelling [11].
- Ability to model complex geometries, with non-linear and anisotropic behaviours [11].
- Excellent for large-scale and transient simulations [11].
- It is a completely explicit method, so it does not use linear algebra, allowing to avoid the limitations imposed by it (no integral equations and no matrix inversions are required).
- It is a time-domain technique, thus if the source is a broadband pulse (as a Gaussian pulse), it is capable to give a system response over a wide range of frequencies with a single simulation; this is useful in applications with unknown resonance frequencies or when result is desired in broadband.

Anyhow the FDTD method has also some disadvantages, mainly:

- Necessity to grid the whole computational domain and the spatial discretization of the grids must be good enough to solve both the smallest electromagnetic wavelengths and the smallest geometric element of the considered model. Consequences are very large computational domain and, an extended time to have the solution of the model.
- Low order of accuracy and stability unless fine grid is used.
- Finite computational domain to allow its storage in the processor memory.
- Rectangular computational meshes makes difficult the application to the curved surfaces, decreasing the system accuracy.

To make finer the grid dimensions and so to improve the accuracy of the simulation, it is possible to implement the FDTD method on a supercomputer, which has a higher level of performance if compared to a general computer.

## 1.2 Time Reversal

This chapter provides an historical background of Time Reversal (TR) technique, presents its basic physics, and summarizes some practical applications. Image to video-record a pebble launched into a pond, generating circular waves that propagates outward from the location at which pebble enters the water, as shown in Figure 5 [12]. At this point, image to stop the movie and project the movie in reverse: the waves will propagate toward the original source location, until they reproduce the point where the pebble broke the surface of the pond and so initial impulse [12]. TR conceptually works in the same way. Meaning that, based on the principle of reciprocity, TR allows a wave to propagate backward to its source. Therefore, TR is a technique capable to focus wave energy, irrespective of whether it is acoustic or electromagnetic, to a specific point in space and time, localize and identify a wave propagation source and/or transmit information between two points [12]. TR concept always fascinated the majority of scientists. Indeed, this kind of physics symmetry can be used for both acoustic waves and electromagnetic waves (more recently), leading to a huge variety of scientific and engineeristic applications. Nowadays, these applications range from medical imaging and therapy to telecommunications, passing through seismology and acoustic testing [13].



*Figure 5 Photograph of ripples propagating outward from the location at which pebble enters the water.*

### ***1.2.1 Historical Background and Applications***

Time reversal first application dates back to 1965, when Parvulescu and Clay studied what they termed “matched signal technique” [13]. Their experiment consisted in the transmission of a signal from a source to a receiver which, after being received, was temporally reversed and broadcast again from a source to a receiver [13]. The use of the matched signal technique allowed to compensate for the distortions on the received signal due to the phenomenon of reverberation (multi-path distortion), giving rise to an increase in the signal-to-noise ratio [13]. Moreover, this process spatially focused the arrival of the waves in space [13]. The activity of researchers between the 1970s and the 1980s led to the creation of a unique mirror, named as Optical Phase Conjugator (OPC). This mirror provided the medium capable of back projecting an incident ray, in exactly the same direction from which it was received [13]. OPCs roughly realize Time Reversal but differentiate from it mainly because they work exclusively with quasi-monochromatic waves, while TR operates in any frequency bandwidth [13]. In 1991, TR was applied in under-water acoustics to correct for multi-path distortions and to obtain a narrow beam, thus improving the focus of the transmitted acoustic energy [13]. This finding provided the means to track moving target. At the beginning of the 1990s, the progress of microelectronics and array technologies, together with the introduction of new theoretical tools, led Fink and his collaborators (at the University of Paris VII, Laboratoire Ondes et Acoustique, LOA) to the development of a device for the acoustic time inversion, named as Time Reversal Mirror (TRM) [13] [14] [15]. Fink et al. noticed that any words spoken in front of an array of microphones and megaphones were played back but in reverse [14]. The echoes of the word "hello" almost instantly became "olleh". The surprising thing was that the sound, instead of being dispersed in the room, was rebroadcast exactly towards the vocal source, as if the time had been reversed [14]. Subsequently, TR has been applied with success in electromagnetic field [16].

Lerosey et al. have overcome the greatest difficulty in transposing TR concept to high frequency electromagnetic waves due to much higher sampling frequencies needed to digitize them with respect to ultrasonic waves. In detail, they have been shown that is possible to time reverse microwaves without fully digitizing them, since the interesting part of a radio frequency modulated signal is its complex envelop [16]. Therefore, TR of this kind of modulated wave is achieved digitizing and time reversing the modulation and phase conjugating the carrier [16] [17]. Recently, TR has been also applied for Electro-Magnetic Compatibility test, to control the interferences between electrical and electronic equipment [18]. Using high reverberating medium, it has been showed a very precise focusing of the wave in space, even with a TRM limited to a single antenna [17]. In the last few years, TR has been finding various applications in the medical field, representing a powerful therapeutic and diagnostic tool. TR is naturally capable to compensate for human body tissues heterogeneity in density and so to avoid waves refraction and scattering phenomena [13]. In fact, during the forward signal propagation the information about the medium are recorded in a TRM [13]. An example of biomedical practical use of TR concerns with the application of TRM's to locate kidney stones and destroy them by focusing high amplitude (lithotripsy therapy) [13]. Other applications in development try to exploit TR focusing through the skull to treat brain tumors with hyperthermia therapy and for brain surgery [19].

### ***1.2.2 Working Principle***

The peculiarity of TR is to offer the capability of focusing a wave on both time and space. Overall, TR consists of a forward propagation step and a backward propagation step. In the forward propagation step, a source emits waves that propagate through a medium, and are then detected at the TRM, accounting for an array of receiving detectors [12]. Detected signals from each transducer are then time-reversed and rebroadcasted from their respective location. Therefore, the traversed wave paths are the same for both forward and backward propagations [12].



Back-propagated waves combine constructively at real source position to reach a maximum. In fact, they simultaneously arrive at the original source location in phase, producing a time reversed focus, which is a reconstruction of the original source [12]. Exploiting the reciprocity theorem, the same signal is acquired by broadcasting a pulse at the TRM and recording the signal at original source point. Indeed, the backpropagation relies on the wave equation reversibility in time. Let return on the case of a peddle dropped in a pond, represent an example of TR in the free space. To perform TR with the aim of exactly duplicate the reversed movie playback, it is required an infinite number of detectors surrounding the drop to exactly detect the ripple motion. Once detected the signals, receivers act as the source of ideally mono-directional sources to reproduce the reversed version of ripples. If only a few detectors are used, the result would be a partial reconstruction of the impulse generated by the launched pebble [12]. Another requirement is that once the reversed ripples reach the contact point, a pebble would have to emerge from the water at the same moment the ripples converge [12]. It is crucial, since ensures that converging ripples does not pass simply through each other, creating again outward ripples again. TR functioning is similar to those beyond the creation of a phased array, also used to concentrate energy at a specific point. The main difference is that phased arrays require introduction of time delays among different transducers so that waves interact and focalize their energy in a specific point [12]. Therefore, it is necessary to accurately compute the slightly different delays in firing transducers, while in TR it is not required such calculation. TR just inverts in time the forward propagation signal and the proper delay are already encoded in it. Nevertheless, all received, reversed and re-emitted signals must be synchronized in time to ensure that encoding is done correctly [12].

### ***1.2.3 Electromagnetic Time Reversal***

As already said, TR theory has been applied for a long time in acoustics/ultrasounds applications and only recently it has had success in the electromagnetic field [16] [20] [21] [22] [23] [24] [25] [26] [27].

Anyhow, Electro Magnetic Time Reversal (EMTR) is still in its early stages and research is ongoing to experimentally validate theoretical and numerical simulations. The basic principle of EMTR is the same as traditional TR. In Figure 6, they are reported the two phases of TR technique [18]. Initially, a source placed at  $R_0$  broadcasts an electromagnetic pulse through the medium. The source can be either active (in case of transmission mode) or passive (as diffraction source). The electromagnetic radiation is detected by an array of receivers ( $R_i$ ) for a period  $\Delta t$ . Receivers are placed around the source in a circular way, forming a Time Reversal Cavity (TRC) [18].

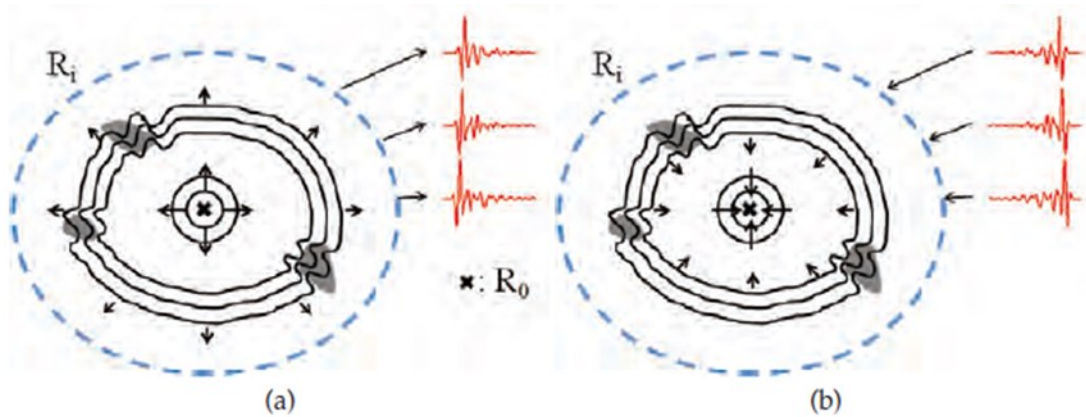


Figure 6 Electromagnetic Time Reversal process with a time reversal cavity: forward propagation and measurement (a), time reversing and back-propagation (b).

First, arriving signals in time travel a shorter distance than later arriving signals. Successively, each detector rebroadcasts received signal in reversed time order, so that those that travel a shorter distance are emitted later, and vice versa. It results a returning wave propagating and acting as if it precisely goes back in time and it leads to spatial and temporal focusing of the wave energy to  $R_0$  in a moment considered as the time origin [18] [20]. TRC is not practically feasible and the usage of large number of probes is highly expensive. Consequently, TR experiments are generally conducted with TRM, made of a limited number of detectors [18]. The principal limitations concern with loss of information causing reduced focus quality, since in the back-propagation step only part of the wave is time-reversed [18]. Figure 7 shows TR phases in TRM.

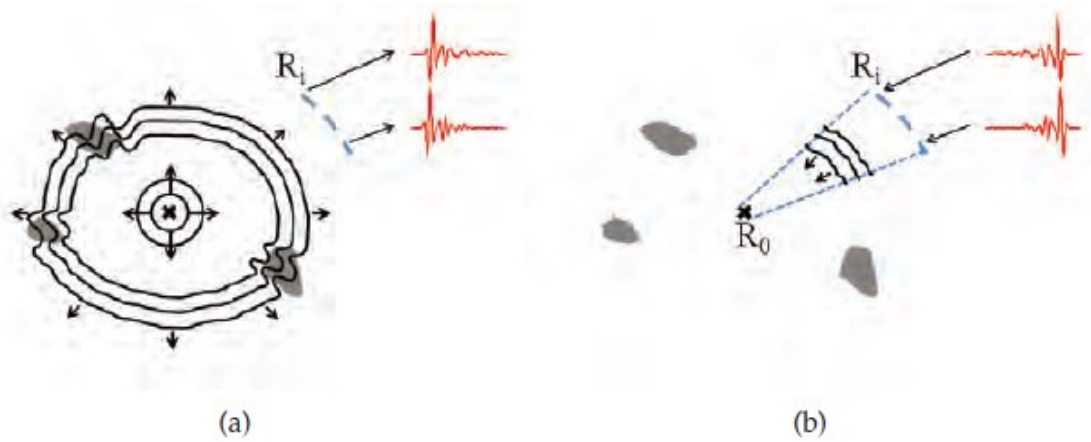


Figure 7 Electromagnetic Time Reversal process with a time reversal mirror: forward propagation and measurement (a), time reversing and back-propagation.

EMTR can be partially improved using a Reverberation chamber (RC), whose characteristics will be explained more in detail in paragraph 1.2.4. Literatures have shown that EMTR application RC can be performed with a single probe instead of an array of probes (Figure 8) [18]. Indeed, RC allows to exploit the several wave reflections on the metal walls, ensuring enough information to be recorded by a single detector [18].

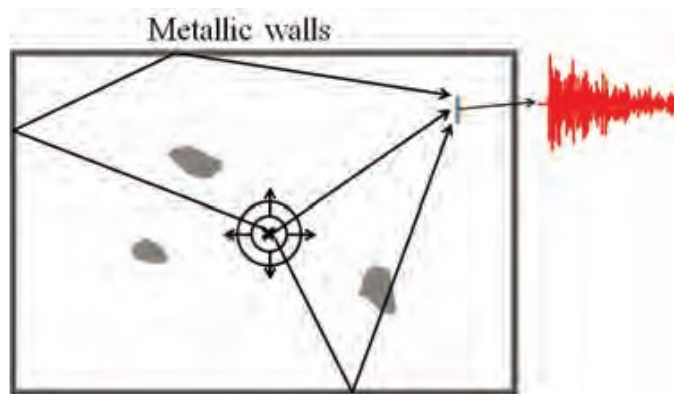


Figure 8 Electromagnetic Time Reversal forward propagation detection with a unique probe in reverberation chamber.

As already mentioned, TR back-propagation is based on the time reversibility of the wave. An electromagnetic propagation medium is named “reversible” if a wave and its time reversed version can propagate through it, so both  $\phi(t)$  and  $\phi(-t)$  are solutions of the same propagation equation [18]. Let consider a non-dissipative and uniform medium. The electromagnetic wave propagation equation through the medium is [18]:

$$\frac{1}{c^2} \frac{\partial^2 \phi}{\partial t^2} = \Delta \phi \quad (30)$$

Where  $\phi$  accounts for E or H and c is the wave propagation velocity into the medium. Considering  $\phi_0(t)$  as a solution of (30), the lack of first time-derivative in the equation left-side leads to the existence of another solution temporally reversed [18]:

$$\phi_1(t) = \phi_0(-t) \quad (31)$$

A consequence is the invariance of (30) with respect to TR application. Thus, an electromagnetic wave propagation can be reversed from time  $t = \Delta t$  to  $t = 0$  seconds [18]. Let consider an E estimated at time t and at point p,  $E(r,t)$ . TR fields data are firstly recorded in a time  $T = \Delta t$ . Then, fields are rebroadcasted during the reversal phase as  $E(r,T-t)$ ,  $t \in [0;T]$  [18]. Overall, considering the Maxwell equations, it has been demonstrated the  $\mathbf{E}$  and  $\mathbf{D}$  are even vectors, instead  $\mathbf{H}$  and  $\mathbf{B}$  are odd vectors during the TR action [18] [20]. Let consider the time inversion operator,  $T_{TR}$ , given by:

$$T_{TR}\{\phi(r, t)\} = \phi(r, -t) \quad (32)$$

From which:

$$T_{TR}\{E(r, t)\} = \phi(r, -t) \quad (33)$$

$$T_{TR}\{D(r, t)\} = \phi(r, -t) \quad (34)$$

$$T_{TR}\{H(r, t)\} = -H(r, -t) \quad (35)$$

$$T_{TR}\{B(r, t)\} = -B(r, -t) \quad (36)$$

Consider the Fourier transform of the field  $\phi(r, t)$  as  $\Phi(r, \omega)$ . It has been demonstrated that signal time reversing coincides to the Inverse Fourier Transform (IFT) of the phase conjugate of its Fourier transform [18]:

$$T_{TR}\{\phi(r, t)\} = \phi(r, -t) = ITF\{\Phi^*(r, \omega)\} \quad (37)$$

### ***1.2.4 Electromagnetic Time Reversal in Reverberation Chamber***

Electromagnetic reverberation chamber (also named reverb chamber or mode-stirred chamber) is an environment for electromagnetic investigations, particularly for EMC testing. EMC test in RC was firstly proposed by H.A. Mendes in 1968, but only after decades of several successful studies the scepticism of a scientific community part, in using a statistically uniform environment for EMC testing, has been overcome [28]. A RC is a screened room, usually of rectangular shape, with perfectly conducting walls (with minimum of electromagnetic waves absorption), as shown in Figure 9. RC is a cavity resonator with high Q factor. Therefore, inside RC the electromagnetic field distribution is marked by a strongly inhomogeneous standing-wave pattern due to the reflection from the walls [28]. According to electromagnetic theory, there are different modes within electromagnetic field, each one describing a certain standing-wave distribution of electromagnetic fields, as shown in Figure 10. The overall field value accounts for the summation of all existing modes inside the chamber [28]. To reduce the inhomogeneities in the electromagnetic field, stirrers (or tuner) are placed inside the room. A stirrer is composed by large metallic reflectors that rotate in several directions in order to continuously alter the boundary conditions of the chamber.

During the stirrer's rotation, all the positions inside the working volume are subjected to wave fluctuation, and it is supposed that they will be subjected to the same maximum, minimum and average electromagnetic field values. If it is so, the chamber is named "well-stirred" and depicts a statistical uniform environment for electromagnetic investigations [28]. Principal advantages of reverberation chamber over traditional anechoic chamber (which stops all wave reflections) concern with lower construction costs (since no absorbers are needed), usage of moderate input power (high conductivity allows for high field levels), provide the most realistic simulation for electronics acting within a cavity (such as a room or an aircraft) and allows FDTD simulations to be applied in a full-wave approach.



*Figure 9 Reverberation chamber at Otto-von-Guericke-University Magdeburg, Germany. On the left side the vertical stirrer mode is placed, ensuring a statistically homogeneous field distribution.*

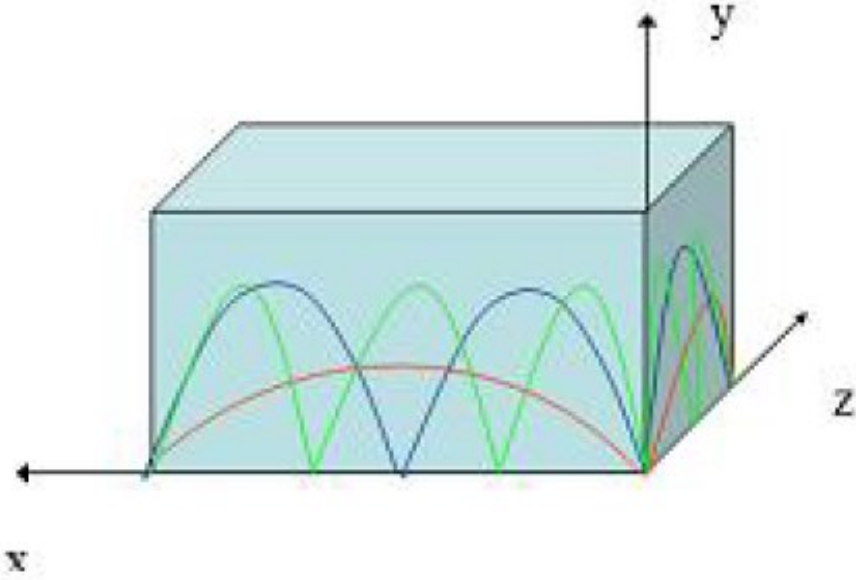


Figure 10 Modes in a rectangular cavity resonator. The goal is to excite as more modes as possible, so that the field within the chamber is a combination of maximums and minimums which tend to be chaotic. Excitable modes enhance with the frequency.

RC allows to improve EMTR since the electromagnetic field description in different modes make the inner environment chaotic enough to ensure a homogeneous distribution of the waves in all directions and improve the focus of the signal. To define an environment as such it must have a number of resonance modes greater than sixty. To do it, it is required to know the dimensions of the room and the resonant frequency of the modes in the rectangular cavity [28]. Resonance frequencies  $f_{mnp}$  are given by:

$$f_{mnp} = \frac{c}{2} \sqrt{\left(\frac{m}{l}\right)^2 + \left(\frac{n}{w}\right)^2 + \left(\frac{p}{h}\right)^2} \quad (38)$$

Where  $c$  is the speed of light,  $l$ ,  $w$  and  $h$  are respectively the cavity's length, width and height and  $m$ ,  $n$  and  $p$  are non-negative integers of resonance, which indicate respectively the axial, tangential and oblique modes (at most one of them could be null) [28].

The empirical formula of the number of modes (N) that resonate at a certain frequency is:

$$N = \frac{8\pi}{3} V \left(\frac{f}{c}\right)^3 - (l + w + h) \left(\frac{f}{c}\right) + \frac{1}{2} \quad (39)$$

In which V is the chamber volume. By introducing a non-linear object, such as a body tissue, the resonant frequency modes increase but the signal due to dissipative effect of tissue is attenuated. Figure 11 gives a representation of EMTR in RC.  $R_0$  is the point source, accounting for the emission antenna, and suppose that it is sending a Gaussian modulated sine pattern pulse [18]. Instead,  $R_i$  is the target point, accounting for the receiving array of probes which is recording the six components of the electromagnetic fields [18]. Then, these signals are reversed by TR or by the phase conjugate Fourier transforms and rebroadcasted by  $R_i$  to achieve both spatial and temporal focusing at  $R_0$  [18].

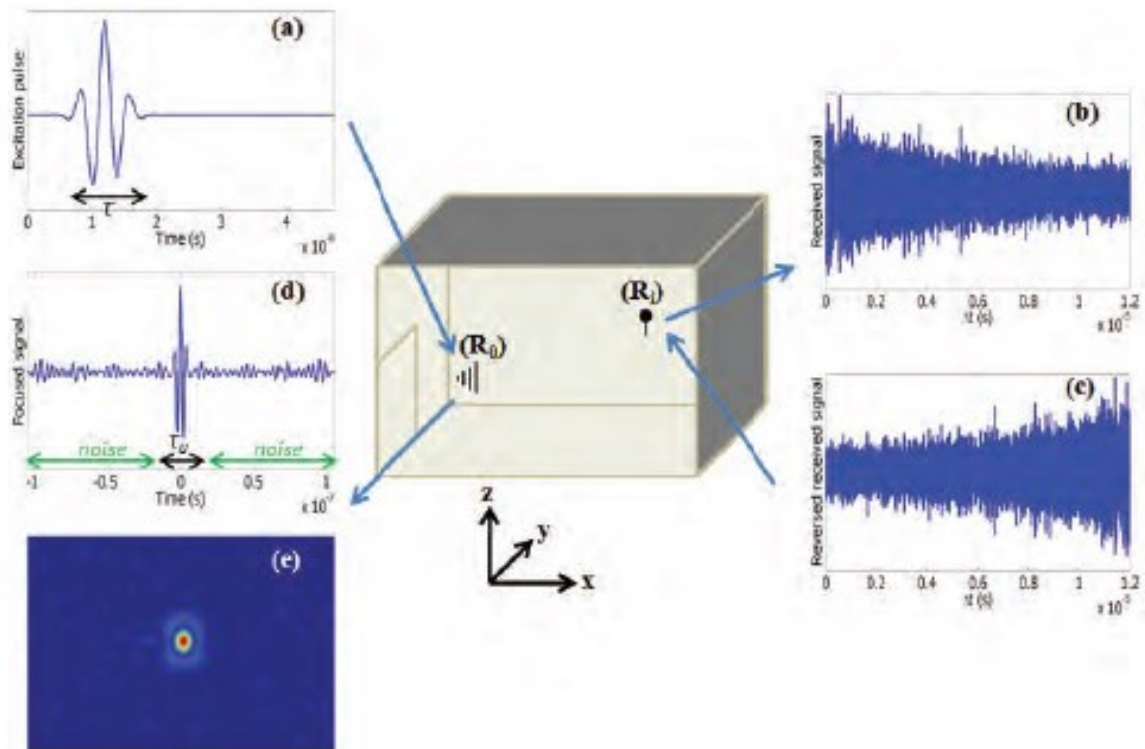


Figure 11 Scheme of electromagnetic time reversal in reverberation chamber: (a) excitation pulse; (b) received signal; (c) reversed received signal; (d) time focusing; (e) space focusing.



The received signal by the array of probes can be written as:

$$y_i(t) = k(t, R_0 \rightarrow R_i) \otimes x(t) \quad (40)$$

Where  $\otimes$  represents the convolution product and  $i$  is an indicator defined as  $1 \leq i \leq M$ , with  $M$  equals to probes number and  $k(t, R_0 \rightarrow R_i)$  is the impulse response of the medium at  $R_i$  for a pulse emitted at  $R_0$  [18]. After TR of  $y_i(t)$  and rebroadcasting of  $R_i$ , the signal focused on  $R_0$  can be written as:

$$\begin{aligned} E_{TR}(t, R_0) &= \sum_{i=1}^M k(t, R_i \rightarrow R_0) \otimes y_i(-t) = \\ &= \sum_{i=1}^M k(t, R_i \rightarrow R_0) \otimes k(-t, R_0 \rightarrow R_i) \otimes x(-t) \end{aligned} \quad (41)$$

Considering that in the frequency domain the convolution product becomes an ordinary product and that a time reversed signal corresponds to the phase conjugate of its Fourier transform [18]:

$$E_{TR}(\omega, R_0) = \sum_{i=1}^M k(\omega, R_i \rightarrow R_0) \cdot k^*(\omega, R_0 \rightarrow R_i) \cdot x^*(\omega) \quad (42)$$

In matrix notation:

$$E_{TR}(\omega, R_0) = K(\omega, R_i \rightarrow R_0) \cdot K^*(\omega, R_0 \rightarrow R_i) \cdot x^*(\omega) \quad (43)$$

Where  $K$  is Fourier transform of several impulse responses between one source and  $M$  receivers [18]. Assuming a reversible medium (allowing a reversible model of the environment), it is possible to apply the reciprocity theorem, which ensures that reversing the point source position with the probe position point, the electromagnetic field is not altered [18].

It means that the impulse from  $R_0$  to  $R_i$  is equal to that from  $R_i$  to  $R_0$ . Therefore, the matrixes  $K(\omega, R_0 \rightarrow R_i)$  and  $K(\omega, R_i \rightarrow R_0)$  are equal, so  $K$  is symmetric [18].

### 1.2.5 Time Reversal in a Linear Time Invariant System

To theoretically describe the EMTR process in a RC, it could be used a Linear Time Invariant system (LTI system). A “system” is defined as any device (or interconnection of devices) which produces an “output” signal that can be measured in relation to an “input” signal. Let consider a system in which to an input  $x(t)$  corresponds a unique well-determined output  $y(t)$  that can be schematized as in Figure 12. The system is subjected on two constraints:

- Linearity, meaning that must be verified the superposition principle. Consider two generic inputs  $x_1(t)$  and  $x_2(t)$  and suppose to know their respective outputs  $y_1(t)$  and  $y_2(t)$  (measured applying input singularly), thus putting as input a linear combination of  $x_1(t)$  and  $x_2(t)$  the output can be obtained by the same linear combination of  $y_1(t)$  and  $y_2(t)$ :

$$x(t) = \alpha x_1(t) + \beta x_2(t) \quad (44)$$

$$y(t) = \Gamma[x(t)] = \alpha y_1(t) + \beta y_2(t) \quad (45)$$

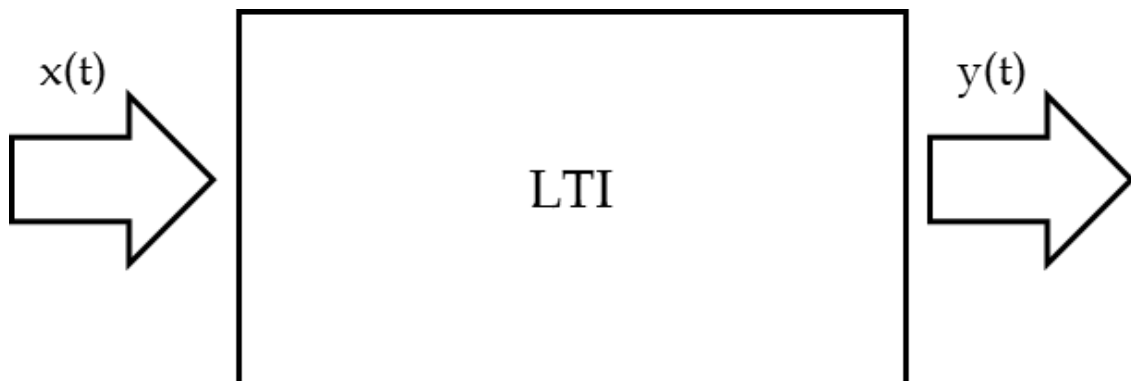


Figure 12 . Linear time-invariant system.

- Time invariance, meaning that the output does not depend on the specific time the input is applied. Applying an input to the system now or at  $t_0$  seconds from now, will give the same output except for a time delay  $t_0$ .

Therefore, if the output due to  $x(t)$  is  $y(t)$ , the output of  $x(t-t_0)$  will be  $y(t-t_0)$ .

The main result is that any LTI system can be described by a single function called the system's impulse response. The system's output  $y(t)$  can be computed as the convolution of the system's input  $x(t)$  with the system's impulse response  $h(t)$ , where the convolution is the mathematical operation defined as the integral of the product of the two functions after one is reversed and shifted:

$$y(t) = x(t) \otimes h(t) = \int_0^{\infty} h(t)x(t - \tau)d\tau \quad (46)$$

Until now the input and output signals have been assumed to be continuous time signals. Actually, the trend is to work on signals in a discrete domain. A discrete-time signal can be obtained from a signal in continuous time by means of sampling operation. A mathematical statement, the "Nyquist-Shannon sampling theorem", says that any waveform made up of several components of different frequencies can be described as a succession of numbers that give the value of the waveform amplitude at intervals determined by the bandwidth of the waveform itself, that is the range of component frequencies, conventionally expressed in Hertz (Hz) or cycles per seconds. In detail, the sampling frequency (the rate with which must be determined the values) must be at least twice the waveform bandwidth to avoid aliasing effect. Thus, sampling consists in extracting from the signal itself the amplitude values it assumes at equally spaced time instants, multiples of an interval  $T$  called the "sampling period". These values will then constitute a sequence whose  $n$ -th value is that assumed by the continuous time signal at instant  $nT$ . Of course, working with discrete signals, the basic mathematical operations change. In particular, considering the convolution for sampled signals, it passes from (44) to:

$$y(t) = x(t) \otimes h(t) = \sum_{j=0}^{N-1} h(j)x(i-j) \quad (47)$$

Then to pass from time-domain to frequency-domain, it is used the Fourier transform (FT). Indeed, instead of considering the actual discrete signal  $x(n)$ , it is considered its FT  $X(f)$ :

$$X(f) = \int_{-\infty}^{\infty} x(t)e^{-2j\pi ft} dt \quad (48)$$

And the transform operation is indicated as follow:

$$x(t) \overset{FT}{\leftrightarrow} X(f) \quad (49)$$

The main advantage of working in the frequency domain is the so-called convolution theorem, which, as already said, states that convolving two signals in time domain is equivalent to making the conventional product of the Fourier transform of the two signals in frequency domain:

$$Y(f) = X(f) \cdot H(f) \quad (50)$$

Considering efficient algorithms as the Fast Fourier Transform (FFT), which computes the discrete Fourier Transform of a sequence, and its reversed form, the Inverse Fast Fourier Transform (IFFT), the following procedure is true:

$$x(t) \overset{FFT}{\leftrightarrow} X(f) \quad (51)$$

$$y(t) \overset{FFT}{\leftrightarrow} Y(f) \quad (52)$$

$$h(t) \xleftrightarrow{FFT} H(f) \quad (53)$$

$$H(f) = \frac{Y(f)}{X(f)} \quad (54)$$

$$y(t) = IFFT[FFT(x) \cdot FFT(h)] \quad (55)$$

$$h(t) = IFFT \left[ \frac{FFT(y)}{FFT(x)} \right] \quad (56)$$

From (54) it is possible to point out that applying a system's input signal  $x(t)$  and measuring the system's output signal  $y(t)$ , to compute the system's impulse response  $h(t)$  it is sufficient to apply the Fourier transform operation to  $x(t)$  and  $y(t)$ , obtaining  $X(f)$  and  $Y(f)$  respectively. The ratio between  $Y(f)$  and  $X(f)$  gives the so called "Transfer Function",  $H(f)$ , which represents the FT of  $h(t)$ . Therefore, applying the IFT to  $H(f)$ , it can be obtained  $h(t)$ . As previously stated, TR consists in the time inversion of the signal. In this case, the system's output signal  $y(t)$  is reversed in time,  $y(-t)$ , and sent as system's input so as to obtain as system's output the signal  $x(t)$ , which had generated the previously output signal  $y(t)$  [29]. The process is schematized in Figure 13.

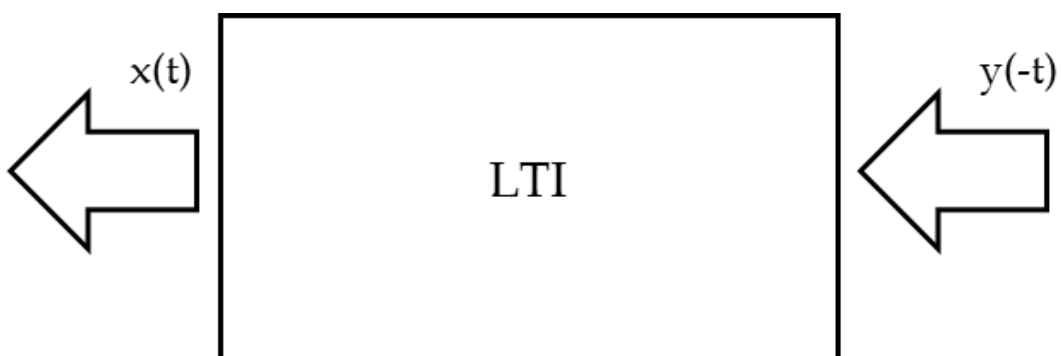


Figure 13 Linear time-invariant system after Time Reversal application.

Considering the fundamental relation (45), it becomes:

$$x(t) = y(-t) \otimes h(t) \quad (57)$$

In the frequency domain it is equivalent to the conventional product of the Fourier transforms of the two signals, where:

$$y(-t) \stackrel{FT}{\leftrightarrow} Y^*(f) \quad (58)$$

Thus:

$$X(f) = Y^*(f) \cdot H(f) \quad (59)$$

Then IFFT is applied to obtain the signal in the time domain:

$$x(t) = IFFT[FFT(y(-t)) \cdot FFT(h)] \quad (60)$$

With time inversion of the signal and with its rebroadcasting, it is possible to focus electromagnetic energy in a specific location in a precise time. This theoretical procedure is adopted for the development of the present thesis.

### 1.3 Dielectric Properties of Body Tissue

Dielectric properties are intrinsic parameters that determine the effect of electromagnetic fields on the matter. Dielectric properties (relative permittivity and effective conductivity) play a key role in study concerning with storage and dissipation of electric and magnetic energy in human body and related application in various disciplines, as electromagnetic dosimetry. This chapter reports a brief overview of the basic dielectric theory, an overall description of body dielectric properties and the illustration of the Cole-Cole equation.

### 1.3.1 Dielectric theory

A dielectric material (or medium) is a very poor conductor of electric current. When a dielectric is placed in an electric field, practically the current flowing in them is null since they have not loosely bound or free electrons that can be exchanged through material (unlike conductor material) [30]. Instead, electric polarization occurs within the dielectric, thus a relative shift of positive and negative electric charges in opposite direction takes place, as shown in Figure 14. In detail, positive charges are displaced in the direction of the electric field, and negative charges place in opposite direction [30]. The slightly separation of charge (polarization) diminishes the electric field within the dielectric. Dielectric materials conditionate other electrical phenomena. For instance, a capacitor filled with a dielectric material has a greater capacitance than it would be in vacuum, and so a greater ability to store opposite charges on opposite plates. The dielectric effects on electrical phenomena are described principally by employing the dielectric constant and permittivity concepts. The dielectric constant (relative permittivity or specific inductive capacity,  $k$ ) is the defined as the ratio of the capacitance of a capacitor filled with the given dielectric material ( $C$ ) and the capacitance of an identical capacitor in a vacuum ( $C_0$ ):

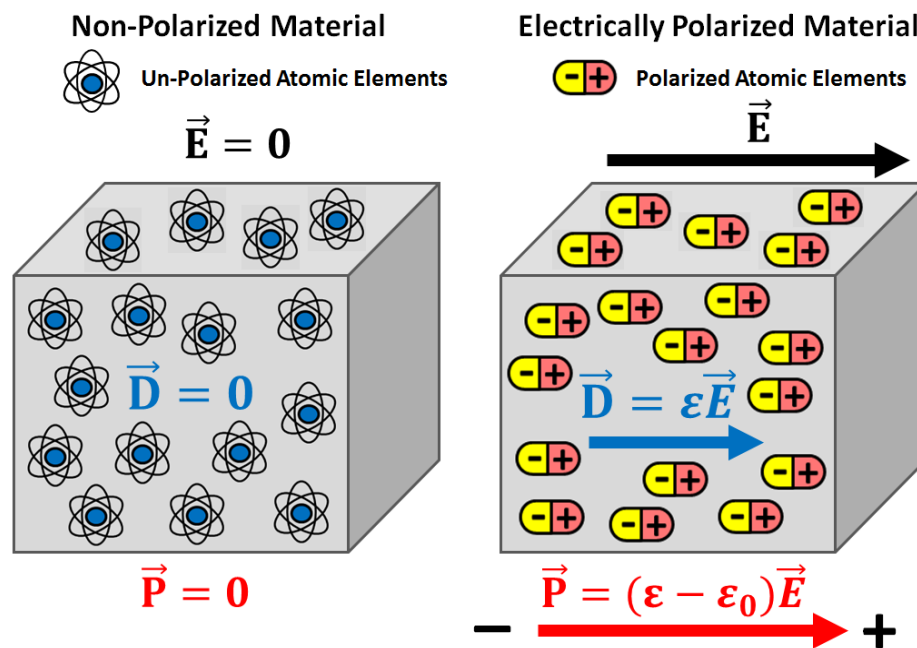


Figure 14 Dielectric polarization verified when a dielectric material is placed in an electric field.

$$k = \frac{C}{C_0} \quad (61)$$

Dielectric constant is dimensionless number and, in the centimetre-gram-second system and it is also defined as:

$$k = \frac{\varepsilon}{\varepsilon_0} \quad (62)$$

Where  $\varepsilon$  is the permittivity, and  $\varepsilon_0$  is the permittivity in the vacuum ( $\varepsilon_0 = 8.854 \cdot 10^{-12} \frac{C^2}{N \cdot m^2}$ ). The permittivity is a constant of proportionality that relates the electric field ( $\mathbf{E}$ ) to the electric displacement in that material ( $\mathbf{D}$ ):

$$\mathbf{D} = \varepsilon \mathbf{E} \quad (63)$$

Therefore  $\varepsilon$  represents the tendency of the atomic charge in a dielectric material to distort in the presence of an electric field [30].

### ***1.3.2 Application in Human Tissue***

Studies of the ways through which human tissues interact with electromagnetic energy are of significant interest in the medical field. The non-ionizing wave ability to penetrate matter and the specificity of electromagnetic properties among the different pathophysiological human tissues have provided the propensity to the study and development of new diagnostic and therapeutic techniques [30]. A possible example is the microwave hyperthermia capable to focus the energy of the microwave field in the cancerous region to induce apoptosis of diseased cell or to locally enhance the chemotherapy/radiotherapy effect. Other applications are related to diagnostic area, as the screening of early breast cancer exploiting the different microwave response of healthy tissue compared to diseased one.



In such contest, the knowledge of dielectric properties human tissues is crucial to understand the interaction between electromagnetic energy and human body. Dielectric properties determine the paths of the current flow through the non-excitabile human tissues, during the exposure to electromagnetic radiation [30]. Human body interacts with electromagnetic field both as bad conductor and bad insulator, so it can reflect, dissipate, and absorbs energy. In this section is considered only the interaction of external electromagnetic field and tissues and not the human intrinsic electromagnetic forces that drive the cell life cycle (mainly related to nervous and cardiac systems) [31]. Dielectric properties of tissues can be described in terms of the effective relative permittivity,  $\varepsilon_{r_{eff}}^*(\omega)$ , of a lossy dielectric material [32]:

$$\varepsilon_{r_{eff}}^*(\omega) = \varepsilon_r'(\omega) - j\left(\varepsilon_r''(\omega) + \frac{\sigma_{dc}}{\omega\varepsilon_0}\right) = \varepsilon_r'(\omega) - j\left(\frac{\sigma_{ac}(\omega) + \sigma_{dc}}{\omega\varepsilon_0}\right) \quad (64)$$

Thus  $\varepsilon_{r_{eff}}^*(\omega)$  is defined as a complex value where the real part is related to the storage of energy and the imaginary part is related to the dissipation of energy and depends on the electrical conductivity of the medium ( $\sigma$ ), representing the medium capacity to conduct current and defined as [32]:

$$\sigma(\omega) = \sigma_{ac}(\omega) + \sigma_{dc} = \omega\varepsilon_0\varepsilon_r''(\omega) + \sigma_{dc} \quad (65)$$

Where  $\sigma_{dc}$  (direct current) represents the ohmic conductivity (from the mobility of ions present in a certain tissue) and  $\sigma_{ac}$  (alternating current) accounts for the losses due to dielectric relaxation (dielectric response of a dielectric medium to an external oscillating electric field) [32]. Biological tissues are uneven between them due to several factors. Consequently, an adequate description of the electrical properties of tissues cannot be based on elementary theoretical models [33]. Dielectric properties are not constant in biological tissues, but changes with external conditions, as temperature and external applied frequency wave [33].

Typically, the relative permittivity of a biological tissue diminishes with increasing frequency in three major steps named as  $\alpha$ -,  $\beta$ - and  $\gamma$ - relaxation, as shown in Figure 15 [25\_Pething]. The  $\alpha$ -relaxation (between 0 and 100 Hz) is generally associated to interfacial polarization due to electrical double layers and surface ionic conduction effects at membrane boundaries [34]. The  $\beta$ -relaxation (between 100 kHz and 100 MHz) is generally described by two components: the capacitive properties of cell membranes in storing the electric charges and the rotational relaxation of biomacromolecules [34]. The  $\gamma$ - relaxation (until 20 GHz) of bulk water in the tissue. For some tissues they may not be clearly distinguishable and furthermore there may be further secondary relaxations. Overall, for all the tissues the real part of the permittivity decreases monotonously as the frequency increases, while the electrical conductivity increases (tissue act as a screen for high frequencies electromagnetic waves). Pething et al have been demonstrate that cancerous tissue exhibits a larger permittivity (as well as a larger conductivity) than normal tissue [34].

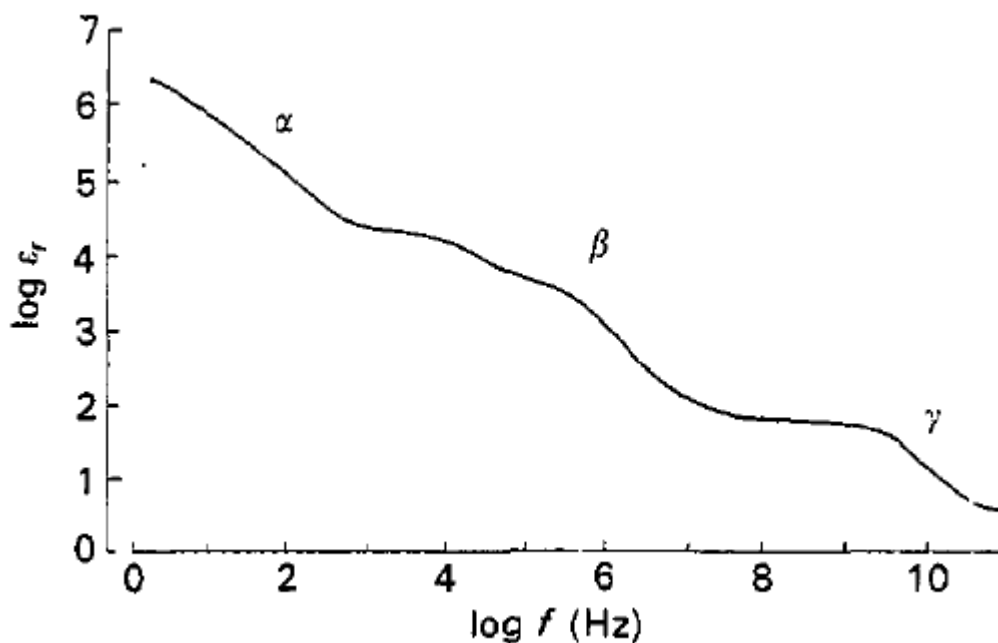


Figure 15 Logarithmic trend of the typical frequency variation of dielectric permittivity real part for a typical biological tissue.

These differences may be related to the fact that cancer cells have a higher water content and sodium concentration than normal cells, and different electrochemical properties of cell membrane [34]. Each dielectric relaxation is based by its own time constant  $\tau$  (dielectric relaxation constant), which can be put in relation to a model that includes the following Debye Equation for the complex relative permittivity [35]:

$$\varepsilon_r^* = \varepsilon_\infty + \frac{\varepsilon_s - \varepsilon_\infty}{1 + j\omega\tau} \quad (66)$$

Where  $\omega = 2\pi f$ ,  $\varepsilon_\infty$  is the permittivity at frequencies for which  $\omega\tau \gg 1$  and  $\varepsilon_s$  is the permittivity at frequencies for which  $\omega\tau \ll 1$  [35]. Dispersion entity is described as  $\Delta\varepsilon = \varepsilon_s - \varepsilon_\infty$ .

### 1.3.3 Cole-Cole Equation

The complexity of both the structure and composition of biological tissues is such that each dispersive region can be breaded by multiple contributions. This extension can be empirically obtained by introducing a distribution parameter  $\alpha$ , used to modify the Debye expression according to the Cole-Cole equation [35]. The model corresponding to the whole spectrum of a tissue is:

$$\varepsilon(\omega) = \varepsilon_\infty + \sum_{n=1}^4 \frac{\Delta\varepsilon_n}{1 + (j\omega\tau_n)^{(1-\alpha_n)}} + \frac{\sigma_i}{j\omega\varepsilon_0} \quad (67)$$

In which,  $\omega = 2\pi f$ ,  $\varepsilon_0 = 8.854 \cdot 10^{-12} \frac{C^2}{N \cdot m^2}$ ,  $\varepsilon_\infty$  is the permittivity in the terahertz ( $10^{12}$  Hz) frequency range,  $\sigma_i$  is the ionic conductivity, for each dispersion region (with  $n := 1 \rightarrow 4$ ),  $\tau$  is the relaxation time and  $\Delta\varepsilon$  is the permittivity drop  $\Delta\varepsilon = \varepsilon_s - \varepsilon_\infty$  · [35] [36] [37]. Choosing appropriate parameters for each tissue, (67) could be used to estimate its dielectric behavior over the considered frequency range [35].

Model parameters were adapted to obtain a best-fit between the model and most likely data set accessible for a particular tissue. The Cole-Cole model delineates dielectric properties in the frequency range from 10 Hz to 100 GHz. It is reliable for frequencies above 1 MHz, but at lower frequencies the model presents not negligible uncertainty [35] [37].

## 2. Thesis Aim

Initially developed for ultrasound, Time Reversal technique has been only recently introduced into electromagnetic area, once overcame the problem related to the much higher sampling frequencies needed to digitize radio frequency signals [16]. It represents a powerful tool in medical field, to the study and development of new diagnostic and therapeutic methodologies. The aim of the present thesis is to conduct a numerical study of time reversal technique in order to achieve both spatial and temporal focusing of electromagnetic fields into a deep point on human head. In detail, numerical simulations are performed using an own-made FDTD code. The numerical modeling of the propagation of the electromagnetic signal and its interaction with biological tissue could provide the tools necessary to a suitable planning of specific therapeutic treatments. For instance, this thesis could serve as basis for experimental research aimed at the design and implementation of applicators based on time reversal technique to focus electromagnetic energy in the diseased tissue, while minimizing the side effects on surrounding healthy tissues.

## 3. Materials and Methods

To reach the purpose of the present study, time reversal is applied in numerical way in order to facilitate its characterization in several configurations. Therefore, an own-made FDTD code is employed to compute the electromagnetic fields into body tissues. FDTD simulations on specific portions of human body are performed according to Virtual Population (ViP) models to correctly describes the relative poses and dielectric properties of tissues under investigation. A gaussian pulse is radiated by a monopole antenna, spread in time due to reverberation, and recorded in the point where we wish to focus electromagnetic energy (carried out by FDTD code). Then, the computed signal is time reversed and rebroadcasted from the same transmitting antenna to converge back in the same target point (focus on both time and space).

### 3.1 Numerical Human Model

In the present study is used a human numerical model from the Virtual Family project [38]. The ViP models are a set of detailed high-resolution anatomical models created from magnetic resonance image data of healthy volunteers. More than 100 different tissue types were distinguished during the segmentation with a resolution of  $1 \times 1 \times 1 \text{ mm}^3$  throughout the entire body [38]. Since their inception, the ViP models have become the gold standard for in silico biophysical modelling applications. All tissues have reconstructed as 3D unstructured triangulated surface objects, producing high precision images of individual body features [38]. For research purposes, the four models provided for free to scientific community are Duke (adult male, 34 years old), Ella (adult female, 26 years old), Billie (young female, 11 years old) and Thelonious (young male, 6 years old) [38]. These four models are referred to as the Virtual Family and are reported in Figure 16 [38]. In Figure 17 is reported a more detailed view of Thelonious' skin, muscles, blood vessels, skeleton, and inner organs [38]. While, in Figure 18 is shown the brain and skull reconstruction of Duke [38].

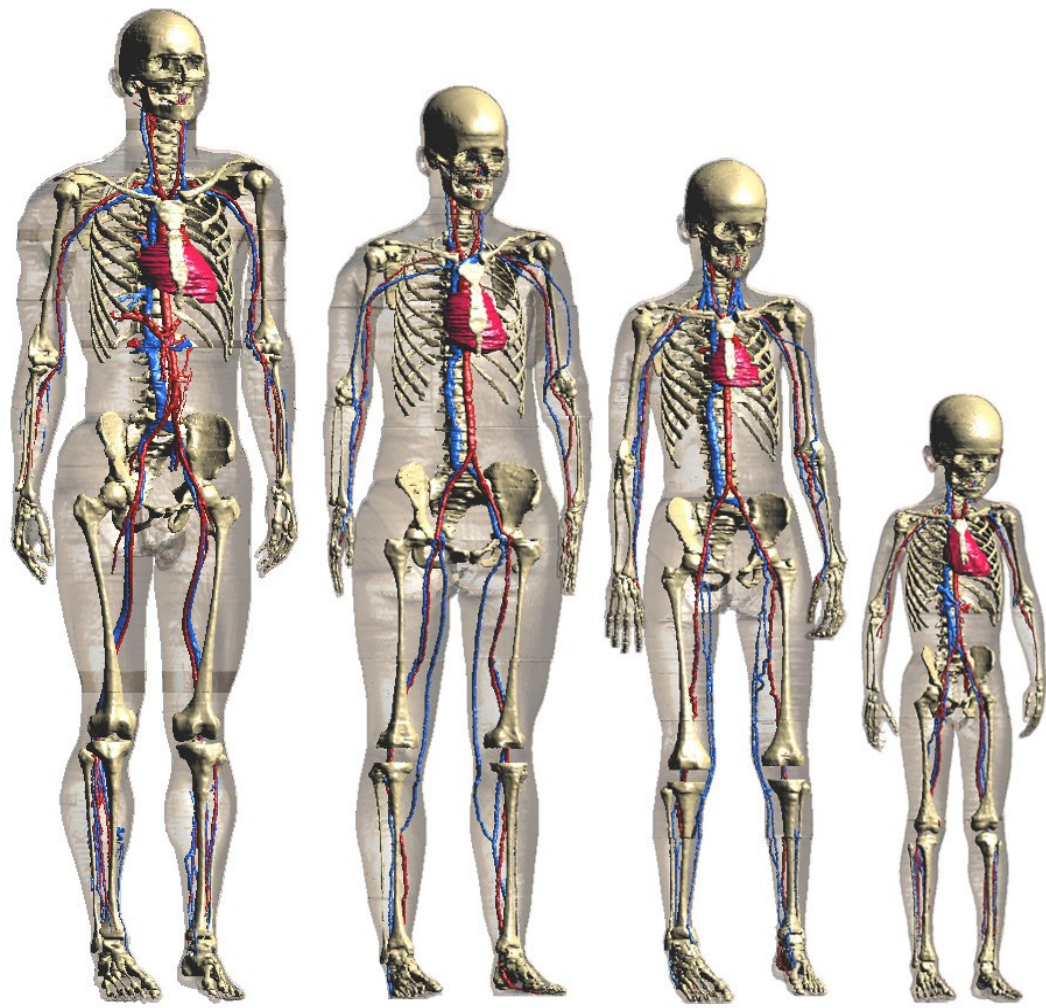


Figure 16 The Virtual Family models. From left to right: Duke, Ella; Billie, Thelonious.

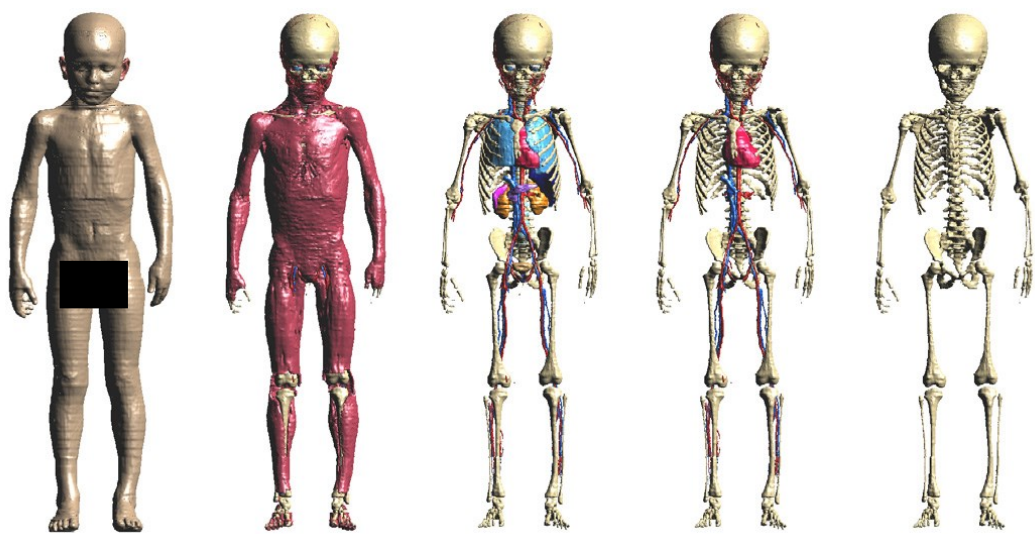
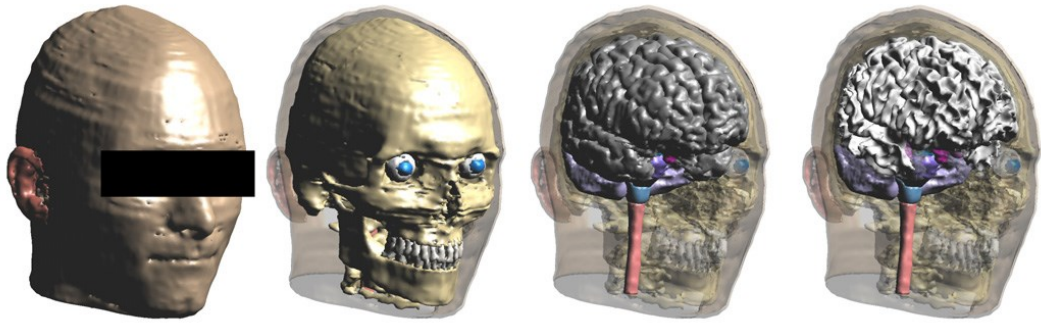


Figure 17 Detailed representation of Thelonious. From left to right: skin, muscle, inner organs, blood vessels and skeleton.



*Figure 18 Duke's head representation. From left to right: skin, skull, brain, and white matter.*

The dielectric parameter values of ViP models are based on tissue dielectric properties database produced by Gabriel et al. [37], which have computed them for a frequency spectrum ranging from a few Hz to several GHz. Since the spectrum under investigation contains four dispersion regions, the values can be fitted using a 4-Cole-Cole dispersion model [paragraph 1.3.3]. The downloaded ViP models are converted from .raw to .vtk file for graphical representation and to .txt file for FDTD. The ASCII format (.txt) is slower and heavier than .raw, but easier to transport to different computers. To view the models is used ParaView, an open-source software for scientific and interactive visualization. For non-homogeneous models, all the tissues are characterized by their complex dielectric constants. For the present analysis is used Thelonious' model, displayed in Figure 19, which has a grid extent (number of cells) equal to  $403 \times 225 \times 1181$  on x, y and z axis respectively, for a total of 107087175 cells. In detail, to carry out FDTD-simulations is used a reduced model of Thelonious, which includes tissues from upper chest to the head, as shown in Figure 20. The reduced model is obtained by cutting cells along the z axis. Finally, the considered number of cells are  $403 \times 225 \times 300$ , respectively on x, y, and z directions, for a total of 27202500 cells.



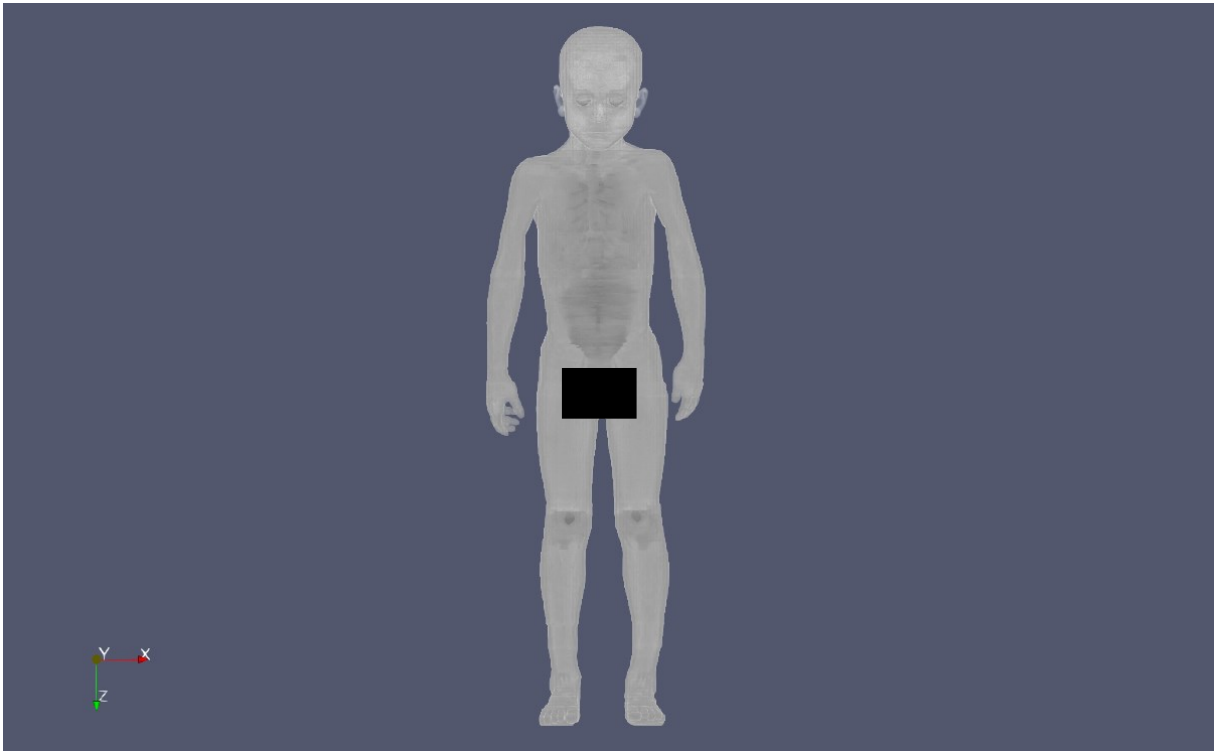


Figure 19 Frontal plane view of Thelonious' model in ParaView software.

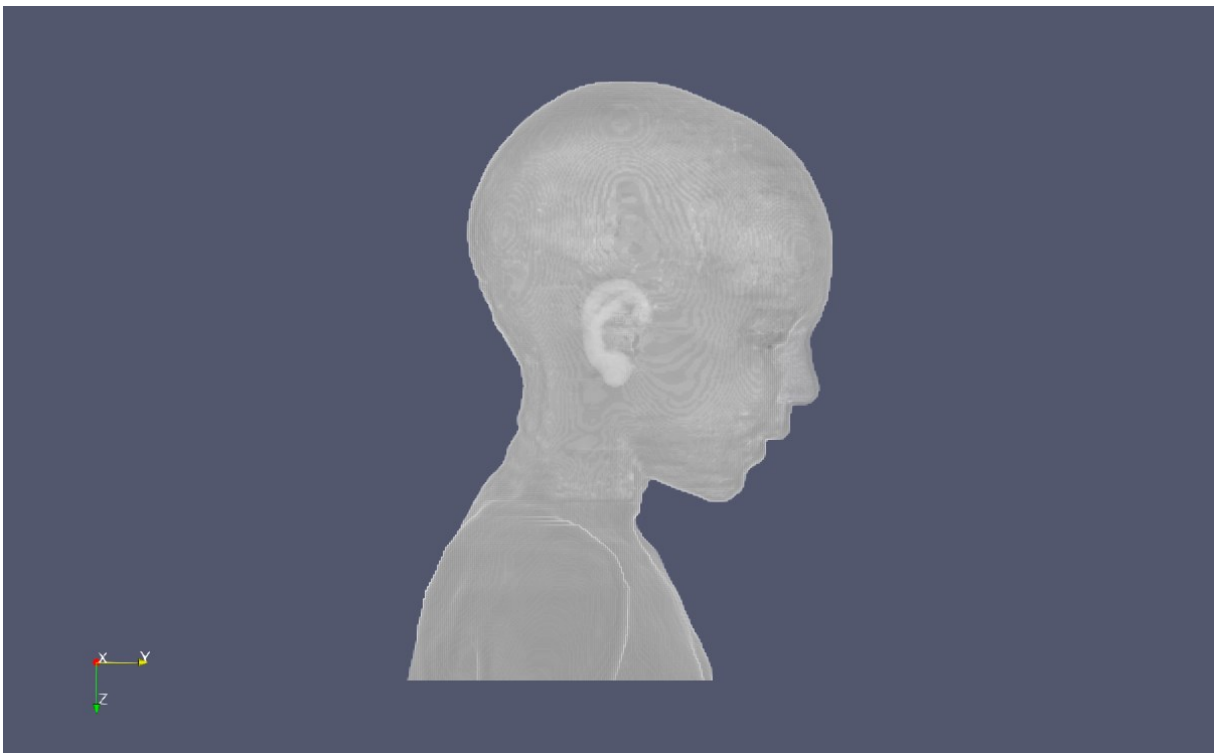


Figure 20 Sagittal plane view of Thelonious' reduced model in ParaView software.

## 3.2 FDTD Modelling of TR

Own-made FDTD electromagnetic code is used to carry out numerical simulations. In detail, it is used KNL Irene (Jolit-Curie), a high-performance computer hosted at Commissariat à l’Energie Atomique et aux énergies alternatives (CEA), France. The code is written in C Language. The already discussed Yee algorithm (paragraph 1.1.2) is implemented to discretize the Maxwell’s equations. These equations are invariant to time reversal transformation. Since the coordinates of the computational grid, on which the differential equations are solved, do not coincide with the coordinates of the model, the tissue properties of the different body regions are assigned to the respective locations of the computational grid (discretizing). Let consider a 2D formulation for simplicity; the 3D case can be easily obtained by extension. In FDTD method, electric and magnetic field are computed by an explicit “leapfrog” scheme considering time intervals separated by half time step. In particular, the electric field at time  $t = n + \frac{1}{2}$  is computed from the electric field at time  $t = n - \frac{1}{2}$  and the magnetic field at time  $t = n + \frac{1}{2}$ , as reported in the discretized Maxwell equations (21), (22), (23), (24), (25) and (26) (see paragraph 1.1.2). To apply the time reversal, we reverse the calculation sequence. Indeed, the electric field at time  $t = n - \frac{1}{2}$  is computed from the electric field at time  $t = n + \frac{1}{2}$  and the magnetic field at time  $t = n$ . This method may only have numerical applications because electromagnetic fields have to be recorded for each discretisation point. In the present study the purpose is not the detection but to focus electromagnetic energy numerically in both space and time. The model used for EMTR in RC allows to avoid field recording throughout the whole domain that should be impossible for experimental future works. In the present study, the pulse is emitted by the source, spread in time due to reverberation and recorded on target point (into the head), during the first phase of TR, using FDTD discretization.

In the second phase, schematized in Figure 21, the computed signal is time reversed and rebroadcasted from the same transmitting antenna to converge back in the same point, and so focus energy on both time and space, without changing the Maxwell's equations in FDTD code.

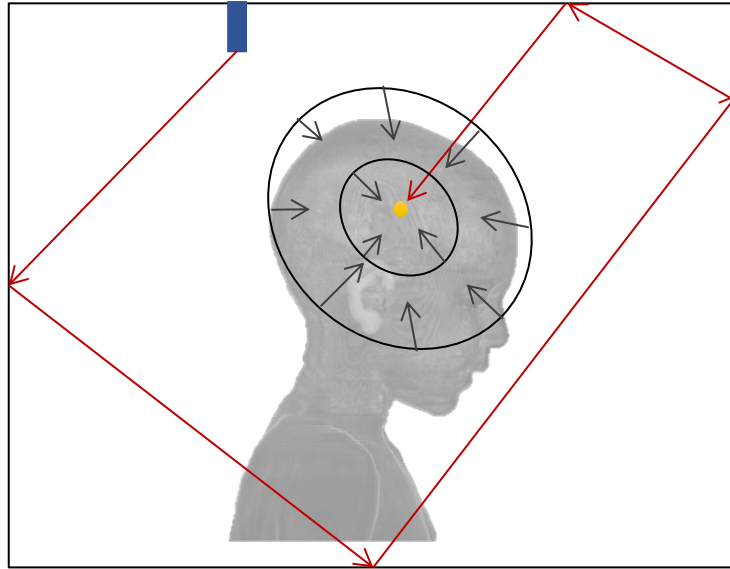


Figure 21 Scheme of second phase of electromagnetic time reversal in reflecting environment: once recorded the signal on the target point (in the head), it is time reversed and rebroadcasted from monopole to target point.

Simulations are performed considering a sinusoidal excitation. In detail, the input signal is a cosine modulated by a Gaussian pulse, at a central frequency of 2.45 GHz, shown in Figure 20 and described as follow:

$$s(t) = \cos(2\pi f_0(t - t_0))e^{-\frac{(t-t_0)^2}{t_g}} \quad (68)$$

In which:

$$t_g = \frac{12}{[\pi(f_{max} - f_{min})^2]} \quad (69)$$

And

$$t_0 = 3\sqrt{t_g} \quad (70)$$

With  $f_{min} = 2.3 \text{ GHz}$ ,  $f_{max} = 2.6 \text{ GHz}$  and  $f_0 = 2.45 \text{ GHz}$ . Therefore, the considered bandwidth is of  $300 \text{ MHz}$ ,  $t_0 = 1.103 \cdot 10^{-8} \text{ s}$  and  $t_g = 1.351 \cdot 10^{-17} \text{ s}$ . The pulse is radiated by a monopole antenna. The monopole antenna is one half of a dipole antenna, generally mounted above some sort of ground plane. This last is the reflective plane, that in this study is represented by a metallic wall composing the reverberation chamber. The component of a monopole (vertical) has a length equal to a quarter of the wavelength of the signal to be transmitted [39]. The monopole is oriented along  $z$  and starting and ending points are respectively placed at  $(x, y, z) = (70, 80, 0)$  and  $(x, y, z) = (70, 80, 22)$  cells from the roof (with respect to the origin of the FDTD domain), so the coaxial cable, which has a total length of  $100 \text{ mm}$ , enters the reverberation box for  $22 \text{ mm}$ , and it is arranged asymmetrically on the lid of the box. The present study is based on four simulations. Simulation I is carried out considering the reduced Thelonious' model into a small reverberation chamber, obtained adding  $80$  cells in both  $x$  and  $y$  directions and  $40$  cells in  $z$  directions. Therefore, the final number of cells are  $483 \times 305 \times 340$ , respectively in  $x$ ,  $y$  and  $z$  directions, corresponding to more than  $50$  million of cells. Simulation II is conducted enhancing the size of reverberation chamber, adding around the reduced model  $400$  cells in both  $x$  and  $y$  directions and  $200$  cells in  $z$  directions. Consequently, the total number of cells is  $603 \times 445 \times 400$  in  $x$ ,  $y$  and  $z$  directions, equivalent to more than  $107$  million of cells. Simulation III is executed considering the same reverberation chamber as in simulation I, but artificially increasing the dielectric permittivity of air into the environment. Hence, outside the reduced model is considered a material with a relative dielectric constant  $\epsilon_r = 36$  and conductivity  $\sigma = 0$ . Simulation IV is performed by including a diffuser into a reverberating environment with equal dimension as that considered in Simulations I and III. The diffuser is made up of two ideal metal plates with dimensions of  $18, 18$  and  $270 \text{ mm}$  respectively along the  $x, y$  and  $z$  axes, and the fulcrum is positioned at  $(x, y) = (463, 285)$  with respect to the origin of the FDTD domain in  $xy$  plane.

### 3.3 Permittivity Value Extraction

The considered Thelonious reduced model file is a voxel model made of more than 27 million cells and containing “char” type data; thus, each character corresponds to a specified tissue. The unit cells of these voxel models have  $1 \times 1 \times 1 \text{ mm}^3$  as volume size, so they are generic cubic model voxel. Then, in each model any “char” element is converted into an “int” element. A function of the own-made FDTD code reads the “int” array of each geometry and assigns to each identification number a tissue. The tissues names and their densities are reported in Table I. The complex dielectric constant  $e(\omega)$  is computed according to the 4-Cole-Cole equation (67), already illustrated in the paragraph 1.3.3. The parameters to compute  $e(\omega)$  for each tissue in a frequency range  $10 \text{ Hz} < f < 100 \text{ GHz}$  are reported in Table II. Table III outlines the relative dielectric constant and conductivity for each tissue, at a frequency  $f = 2.45 \text{ GHz}$  and a temperature  $T = 37 \text{ }^\circ\text{C}$ . Considering the relative dielectric constant and conductivity as constant values at a frequency of 2.45 GHz and not variable in the whole 300 MHz band under investigation, allow to considerably reduce the computational effort and, in turn, the simulations times.

Table 1 Human tissues and their densities.

#	Tissue name	$\rho(kg/m^3)$
0	Air	1.2
1	Blood	1049.7
2	Blood Vessel Wall	1101.5
3	Bone	1908.0
4	Bone Marrow (Red)	1028.5
5	Brain (Gray Matter)	1044.5
6	Brain (White Matter)	1041.0
7	Cartilage	1099.5
8	Cerebellum	1045.0
9	Cerebrospinal Fluid	1007.0
10	Commissure	1041.0
11	Connective Tissue	1525.0
12	Esophagus	1040.0
13	Esophagus Lumen	1.2
14	Eye (Cornea)	1050.5
15	Eye (Lens)	1075.5
16	Eye (Sclera)	1032.0
17	Eye (Vitreous Humour)	1004.5
18	Fat	911.0
19	Hippocampus	1044.5
20	Hypophysis	1053.0
21	Hypothalamus	1053.0
22	Intervertebral Disc	1099.5
23	Larynx	1099.5
24	Mandible	1908.0
25	Medulla Oblongata	1045.5
26	Midbrain	1045.5
27	Mucous Membrane	1102.0
28	Muscle	1090.4
29	Nerve	1075.0
30	Pharynx	1.2
31	Pineal Body	1053.0
32	Pons	1045.5
33	SAT (Subcutaneous Fat)	911.0
34	Skin	1109.0
35	Skull	1908.0
36	Spinal Cord	1075.0
37	Tendon\Ligament	1142.0
38	Thalamus	1044.5
39	Tongue	1090.4
40	Tooth	2180.0
41	Trachea	1080.0
42	Trachea Lumen	1.2
43	Vertebrae	1908.0

Table 2 Parameters to assess to compute the complex dielectric constant for body tissues

#	$\epsilon_{\infty}$ (F/m)	$\Delta\epsilon_1$ (F/m)	$\tau_1$ (ps)	$\alpha_1$	$\Delta\epsilon_2$ (F/m)	$\tau_2$ (ns)	$\alpha_2$	$\sigma_{1-4}$ (S/m)	$\Delta\epsilon_3$ (F/m)	$\tau_3$ ( $\mu$ s)	$\alpha_3$	$\Delta\epsilon_4$ (F/m)	$\tau_4$ (ns)	$\alpha_4$
0	1	0	0	0	0	0	0	0	0	0	0	0	0	0
1	4	56	8.377	0.1	5200	132.629	0.1	0.7	0	159.155	0.2	0	15.915	0
2	4	40	8.842	0.1	50	3.183	0.1	0.25	100000	159.155	0.2	10000000	1.592	0
3	2.5	10	13.263	0.2	180	79.577	0.2	0.02	5000	159.155	0.2	100000	15.915	0
4	2.5	9	14.469	0.2	80	15.915	0.1	0.1	10000	1591.549	0.1	2000000	15.915	0.1
5	4	45	7.958	0.1	400	15.915	0.15	0.02	200000	106.103	0.22	45000000	5.305	0
6	4	32	7.958	0.1	100	7.958	0.1	0.02	40000	53.052	0.3	35000000	7.958	0.02
7	4	38	13.263	0.15	2500	144.686	0.15	0.15	100000	318.31	0.1	40000000	15.915	0
8	4	40	7.958	0.1	700	15.915	0.15	0.04	200000	106.103	0.22	45000000	5.305	0
9	4	65	7.958	0.1	40	1.592	0	2	0	159.155	0	0	15.915	0
10	4	32	7.958	0.1	100	7.958	0.1	0.02	40000	53.052	0.3	35000000	7.958	0.02
11	4	42	12.243	0.1	60	6.366	0.1	0.25	60000	318.31	0.22	20000000	1.326	0
12	4	60	7.958	0.1	2000	79.577	0.1	0.5	100000	159.155	0.2	40000000	15.915	0
13	1	0	0	0	0	0	0	0	0	0	0	0	0	0
14	4	48	7.958	0.1	4000	159.155	0.05	0.4	100000	15.915	0.2	40000000	15.915	0
15	3	32	8.842	0.1	100	10.61	0.2	0.2	1000	15.915	0.2	5000	15.915	0
16	4	50	7.958	0.1	4000	159.155	0.1	0.5	100000	159.155	0.2	5000000	15.915	0
17	4	65	7.234	0	30	159.155	0.1	1.5	0	159.155	0	0	15.915	0
18	2.5	9	7.958	0.2	35	15.915	0.1	0.035	33000	159.155	0.05	10000000	15.915	0.01
19	4	45	7.958	0.1	400	15.915	0.15	0.02	200000	106.103	0.22	45000000	5.305	0
20	4	55	7.958	0.1	2500	159.155	0.1	0.5	100000	159.155	0.2	40000000	15.915	0
21	4	55	7.958	0.1	2500	159.155	0.1	0.5	100000	159.155	0.2	40000000	15.915	0
22	4	38	13.263	0.15	2500	144.686	0.15	0.15	100000	318.31	0.1	40000000	15.915	0
23	4	38	13.263	0.15	2500	144.686	0.15	0.15	100000	318.31	0.1	40000000	15.915	0
24	2.5	10	13.263	0.2	180	79.577	0.2	0.02	5000	159.155	0.2	100000	15.915	0
25	4	40	7.958	0.1	700	15.915	0.15	0.04	200000	106.103	0.22	45000000	5.305	0
26	4	40	7.958	0.1	700	15.915	0.15	0.04	200000	106.103	0.22	45000000	5.305	0
27	4	39	7.958	0.1	280	79.577	0	0.0004	30000	1.592	0.16	30000	1.592	0.2
28	4	50	7.234	0.1	7000	353.678	0.1	0.2	1200000	318.31	0.1	25000000	2.274	0
29	4	26	7.958	0.1	500	106.103	0.15	0.006	70000	15.915	0.2	40000000	15.915	0
30	1	0	0	0	0	0	0	0	0	0	0	0	0	0
31	4	55	7.958	0.1	2500	159.155	0.1	0.5	100000	159.155	0.2	40000000	15.915	0
32	4	40	7.958	0.1	700	15.915	0.15	0.04	200000	106.103	0.22	45000000	5.305	0
33	2.5	9	7.958	0.2	35	15.915	0.1	0.035	33000	159.155	0.05	10000000	15.915	0.01
34	4	32	7.234	0	1100	32.481	0.2	0.0002	0	159.155	0.2	0	15.915	0.2
35	2.5	10	13.263	0.2	180	79.577	0.2	0.02	5000	159.155	0.2	100000	15.915	0
36	4	26	7.958	0.1	500	106.103	0.15	0.006	70000	15.915	0.2	40000000	15.915	0
37	4	42	12.243	0.1	60	6.366	0.1	0.25	60000	318.31	0.22	20000000	1.326	0
38	4	45	7.958	0.1	400	15.915	0.15	0.02	200000	106.103	0.22	45000000	5.305	0
39	4	50	7.958	0.1	4000	159.155	0.1	0.25	100000	159.155	0.2	40000000	15.915	0
40	2.5	10	13.263	0.2	180	79.577	0.2	0.02	5000	159.155	0.2	100000	15.915	0
41	2.5	38	7.958	0.1	400	63.662	0.1	0.3	50000	15.915	0.2	1000000	15.915	0
42	1	0	0	0	0	0	0	0	0	0	0	0	0	0
43	2.5	10	13.263	0.2	180	79.577	0.2	0.02	5000	159.155	0.2	100000	15.915	0

Table 3 Dielectric constant and conductivity for studied human tissues.

#	$\epsilon_r$	$\sigma(S/m)$
0	1	0
1	58.2636	2.5448
2	42.5313	1.4353
3	11.3809	0.3943
4	10.3083	0.4588
5	48.9115	1.8077
6	36.1666	1.2149
7	38.7702	1.7558
8	44.8041	2.1014
9	66.2433	3.4578
10	36.1666	1.2149
11	43.121	1.6847
12	62.1584	2.2105
13	1	0
14	51.6149	2.2954
15	33.9735	1.0869
16	52.6278	2.0331
17	68.2080	2.4780
18	10.8205	0.2679
19	48.9115	1.8077
20	57.2005	1.9679
21	57.2005	1.9679
22	38.7702	1.7558
23	38.7702	1.7558
24	11.3809	0.3943
25	44.8041	2.1014
26	44.8041	2.1014
27	42.8526	1.5919
28	52.7295	1.7387
29	30.1454	1.0885
30	1	0
31	57.2005	1.9679
32	44.8041	2.1014
33	10.8205	0.2679
34	38.0066	1.4640
35	11.3809	0.3943
36	30.1454	1.0885
37	43.1210	1.6847
38	48.9115	1.8077
39	52.6278	1.8026
40	11.3809	0.3943
41	39.7328	1.4488
42	1	0
43	11.3809	0.3943



## 4. Results and Discussion

The mesh of FDTD is uniform and the cell size is  $1 \times 1 \times 1 \text{ mm}^3$ , equal to the dimension of the unit-cell of the used voxel models. The time step is  $dt = 1.9 \text{ ps}$ , enough to satisfy the stability condition, that depends on the medium in which the wave propagates fastest and on the size of the cell (which is constant). Indeed, the maximum value of stability factor is 0.986, less than 1. Before running the simulations, are also checked the minimum stability factor for the fictitious one-dimensional transmission line (always less than 1) and the minimum ratio between the wavelength (122.45 mm at 2.45 GHz) and the cell size (greater than 10). These checks ensure the convergence of the system. Simulation I is characterized by a total number of time iterations equal to 77379 corresponding to a gaussian bell extension of 40 times. In Figure 22 are reported the input (original) signal, which is the signal on the transmission line that is connected to the antenna, and the received signal at the target point (into the head). The original signal is a voltage (in V), instead the received signal on the head is an electric field (in V/m), thus we normalize them because we can compare the shape, not the amplitudes, that are obtained from the power transmitted from the arbitrary signal generator. Being the system linear, only a scale factor must be introduced. Since the monopole has its active part along z axis of 3D space, henceforth we refer to z component of the received signal. We can notice a certain elongation of the signal due to multiple reflections which, however, decays quickly. This is due to the small reverberant cavity, and thus few wave modes and a lot of losses. Then we take the received signal, we reverse (reconstruct) it in time, and we input it to the simulator through the same transmitting monopole. In Figure 23 is depicted the comparison between the original signal and the reconstructed one. We can stress out that the gaussian pulse is well-reconstructed but there are external oscillations (side lobes), since there is not a good reverberant environment. To better quantify the differences among the two signals, we reverse in time the original signal and overlap it to reconstructed signal, as illustrated in Figure 24.

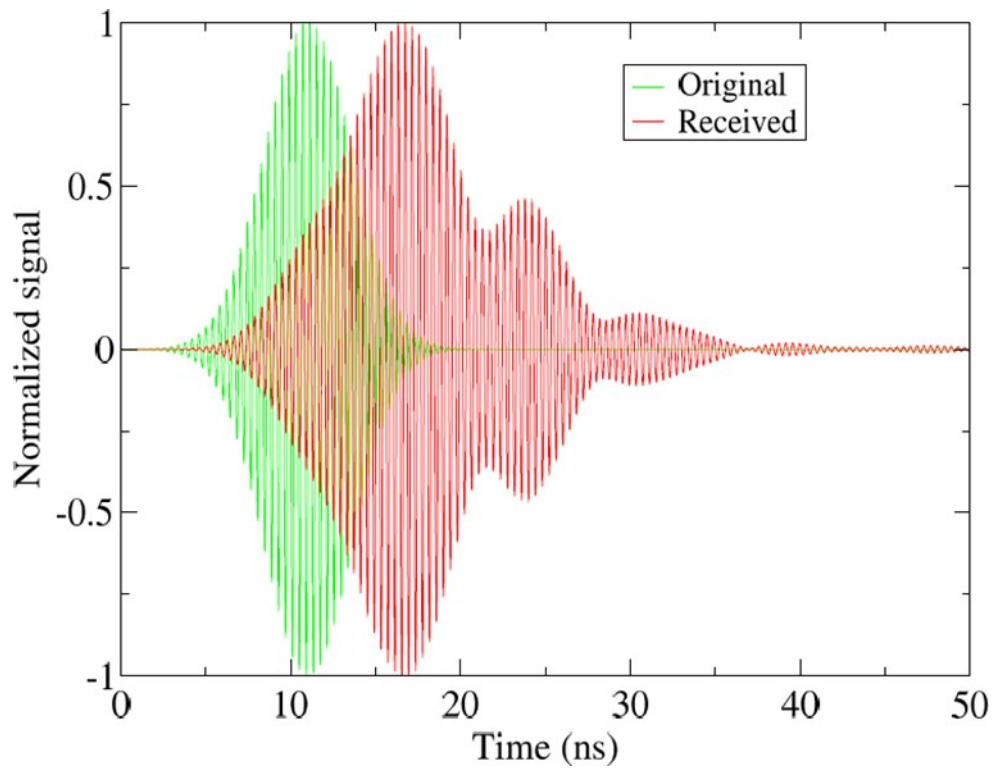


Figure 22 Comparison between the original input gaussian pulse signal centered at 2.45 GHz (with a bandwidth of 300 MHz) and the received signal on the target point (Simulation I). Both signals are normalized to their maximum values.

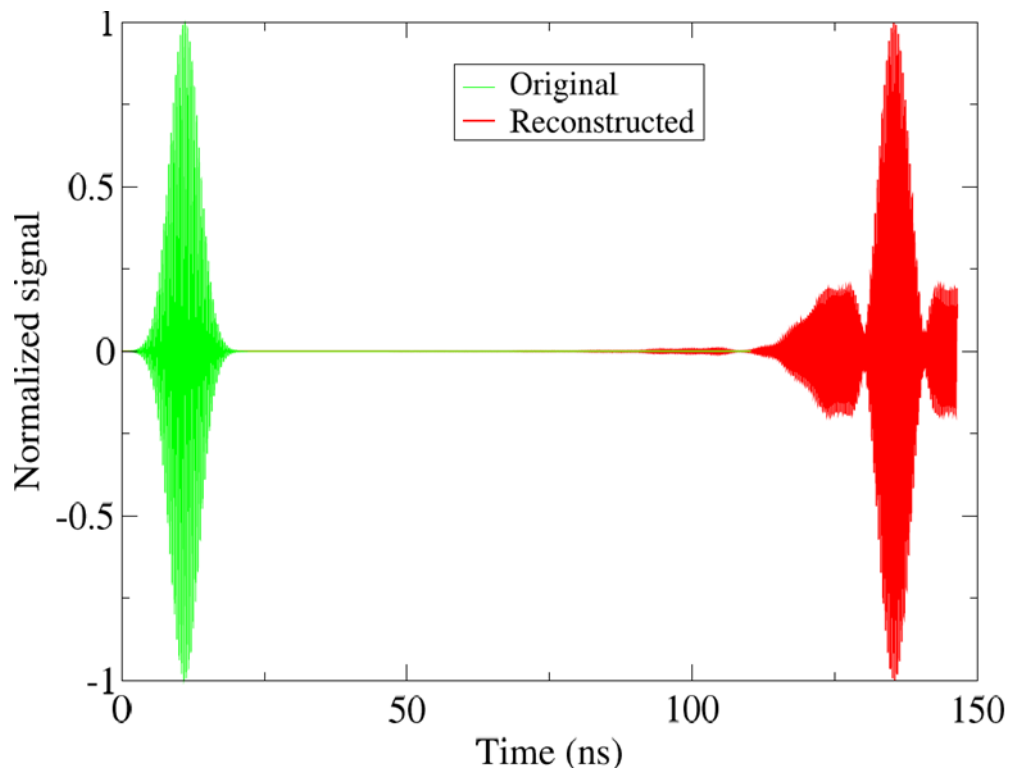


Figure 23 Original signal vs reconstructed signal (Simulation I).

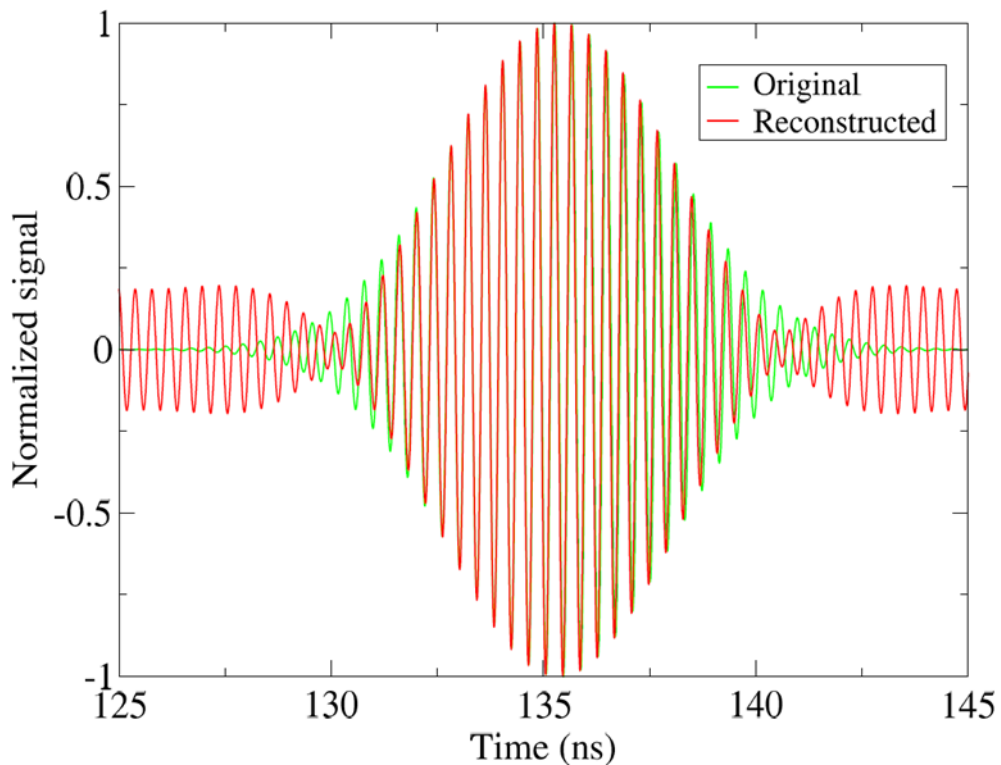


Figure 24 Original signal overlapped to the reconstructed signal (Simulation I).

Simulation I is performed in order to test the validity of the procedure in a short time (less than two hours). To improve the results, we proceed by increasing the size of the reverberation chamber. Simulation II is also marked by a total number of time iterations equal to 77379 as Simulation I, corresponding to a gaussian bell extension of 40 times. In Figure 25 is illustrated the matching between the original signal and the reversed one. In this case, we can observe a longer time decay of reconstructed signal with respect to that of Simulation I. It is a consequence of the increase of reverberation chamber size (working volume) and, in turn, of an increase of the Q-factor. To verify that all the components of electric fields are excited, in Figure 26 we plot the three cartesian components of the received signal at the target point. We can state that the trends are similar, but they vary according to the type of simulations (i.e., kind/position of antenna, target point position, etc.). Figure 27 shows the comparison between the original signal and the reconstructed one, always considering both signals normalized with respect to their maximum values. The original signal is reversed and overlapped to reconstructed signal, as depicted in Figure 28.

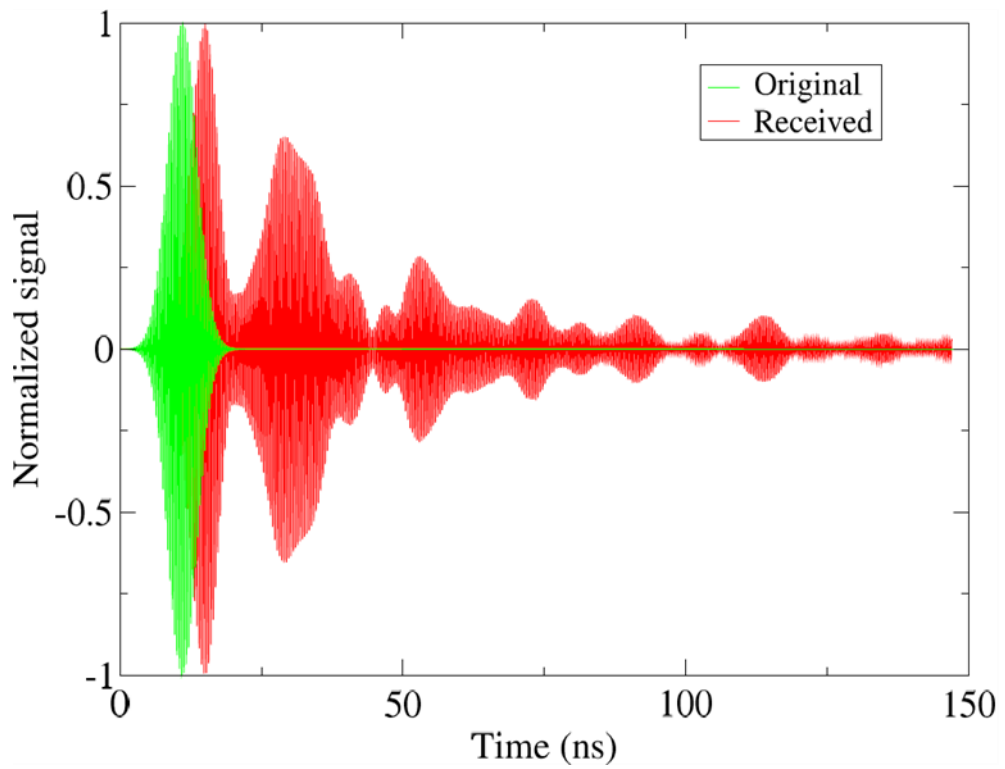


Figure 25 Original vs received signal (Simulation II).

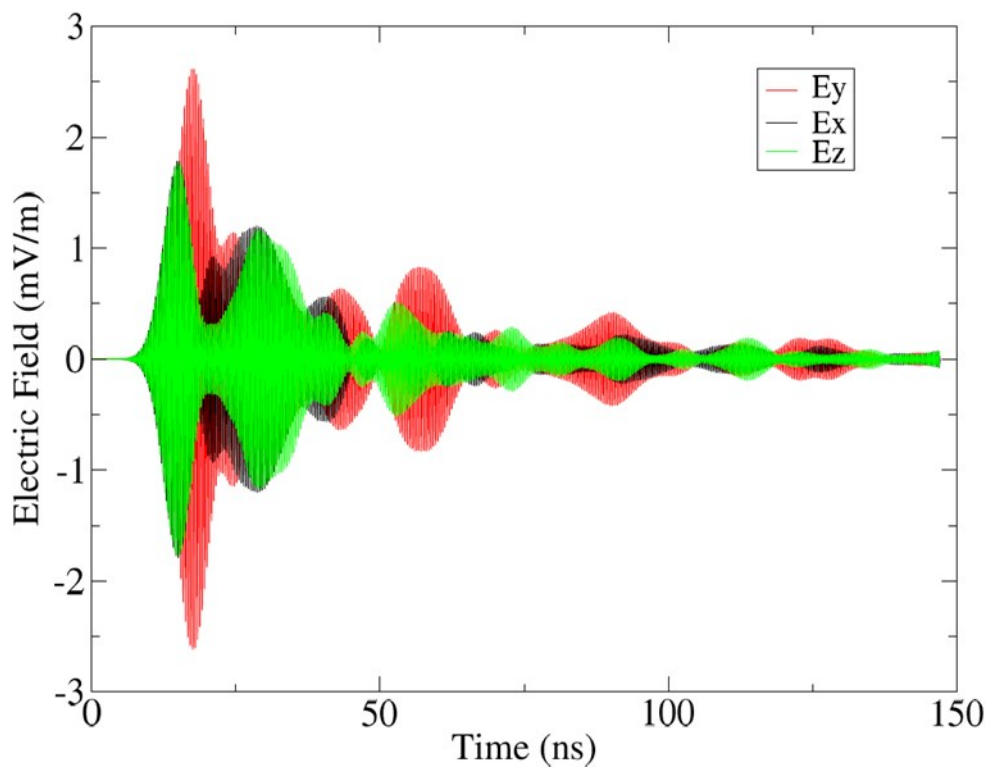


Figure 26 Cartesian components of received signal at target point (Simulation II).

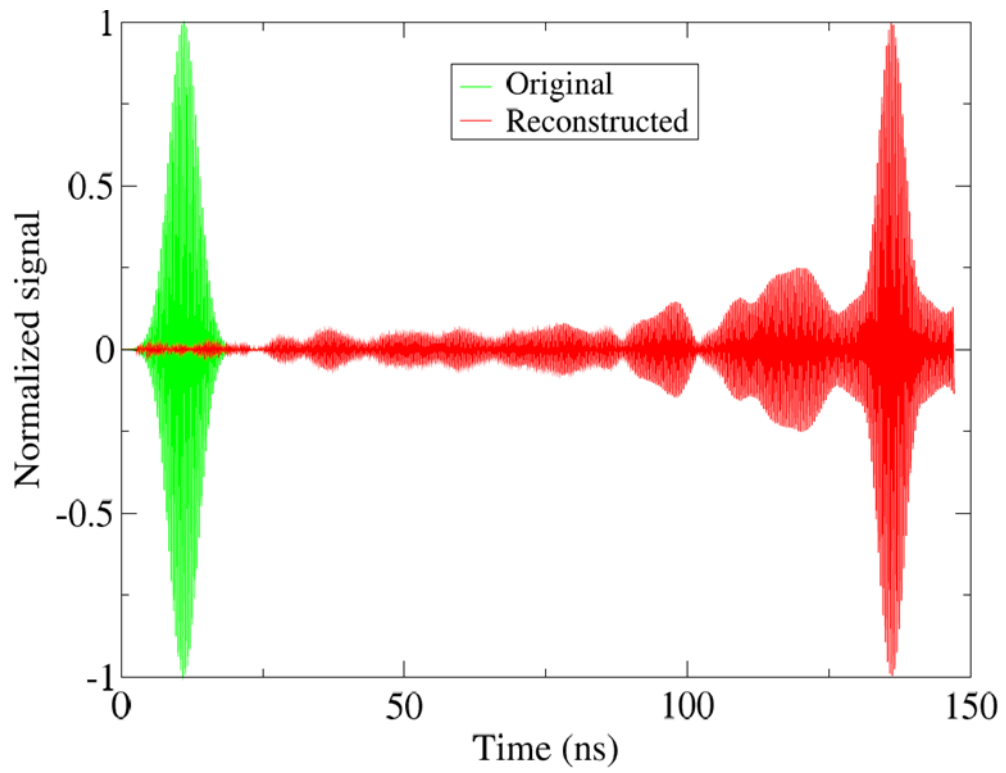


Figure 27 Original signal vs reconstructed signal (Simulation II).

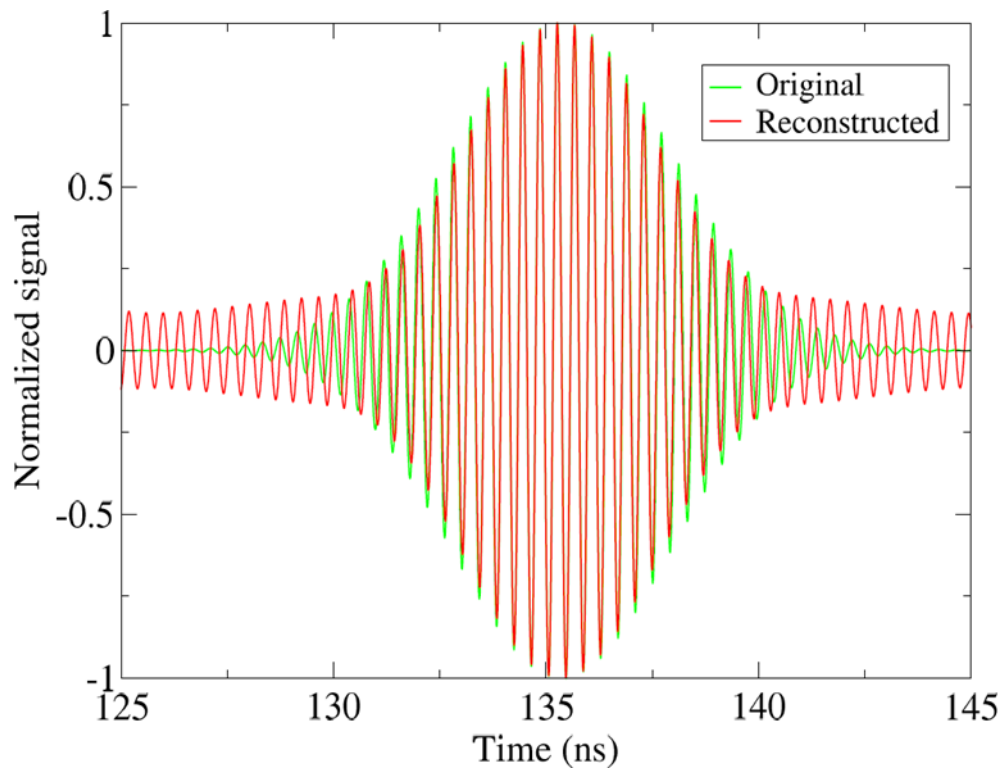


Figure 28 Original signal overlapped to the reconstructed signal (Simulation II).

We can state that enlarging the reverberant environment appreciably enhances the system's ability to reconstruct the original signal, but also greatly increases the computational effort and, in turn, the simulation time (more than eight times with respect to Simulation I). Consequently, Simulation III is based on the same reverberation environment as in Simulation I, but we artificially increase the relative permittivity of the air. It allows to simulate a larger cavity than it actually is, since it causes an enhancement of wave modes number and generates a more chaotic environment while maintaining short computational effort. To avoid problems that can cause divergence of the system, we leave air in a neighbourhood between the junction of coaxial cable and 3D space. Simulation III has a total number of iterations equal to 193449 corresponding to a gaussian bell extension of 100 times. We obtain an enhancement of the chaoticity of the received electromagnetic signal, according to Figure 29. Indeed, it presents an increase of constructive interferences due to multiple reflections that generate an amplification of the signal with respect to the transmitted one. Figure 30 reports both the transmitted and the reconstructed signal. An increase in the decay time of the reconstructed signal and consequently an increase in the Q-factor of the reverberating cavity can be observed. Figure 31 displays the transmitted signal overlapped to the reconstructed one. The times shown are greater than in the first two simulations because the signal lasts longer over time. The increasing of oscillations and chaoticity could be due to the presence of air around the monopole which acts as diffuser. An improvement of side lobes filtering is evident, but a slight worsening in the reconstruction of the main beam is also perceptible. Anyhow, Simulation III requires a considerably lower memory space than that required for Simulation II. It accounts for a good trade-off between quality of the results and calculation times (about four times lower than those of Simulation II). Finally, we add a diffuser to further increase the chaoticity of the working volume. The diffuser is rotated of about  $30^\circ$  with respect to the metallic walls to avoid any geometric symmetry and, thus, enhance the number of wave modes. Simulation IV is characterized by a total number of time iterations equal to 193449 corresponding to a gaussian bell extension of 100 times.

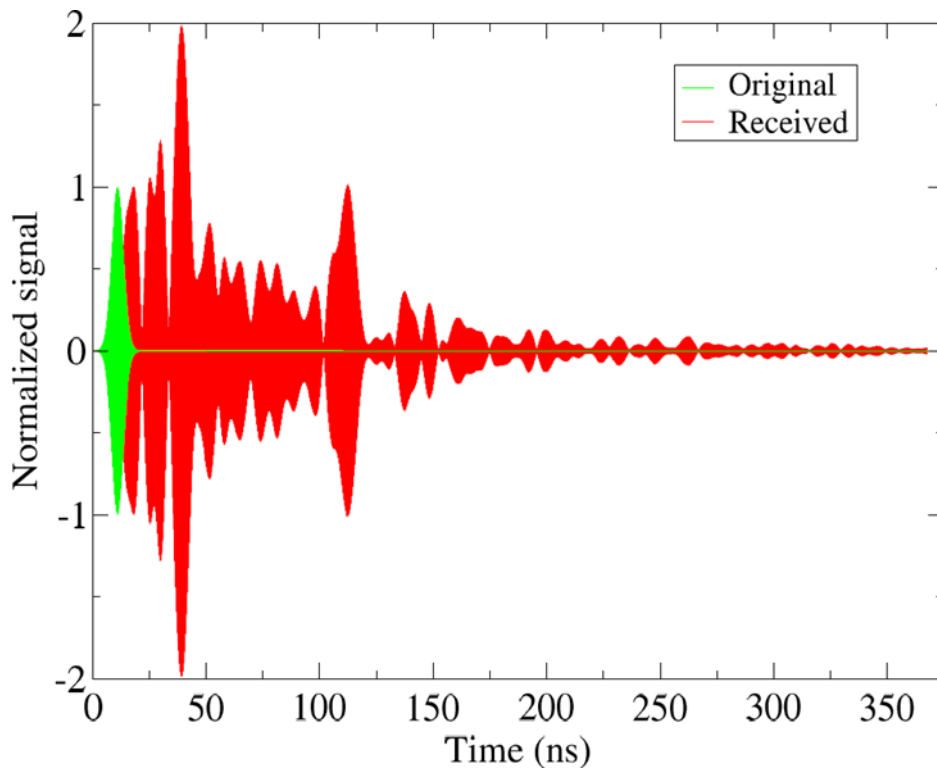


Figure 29 Original vs received signal (Simulation III).

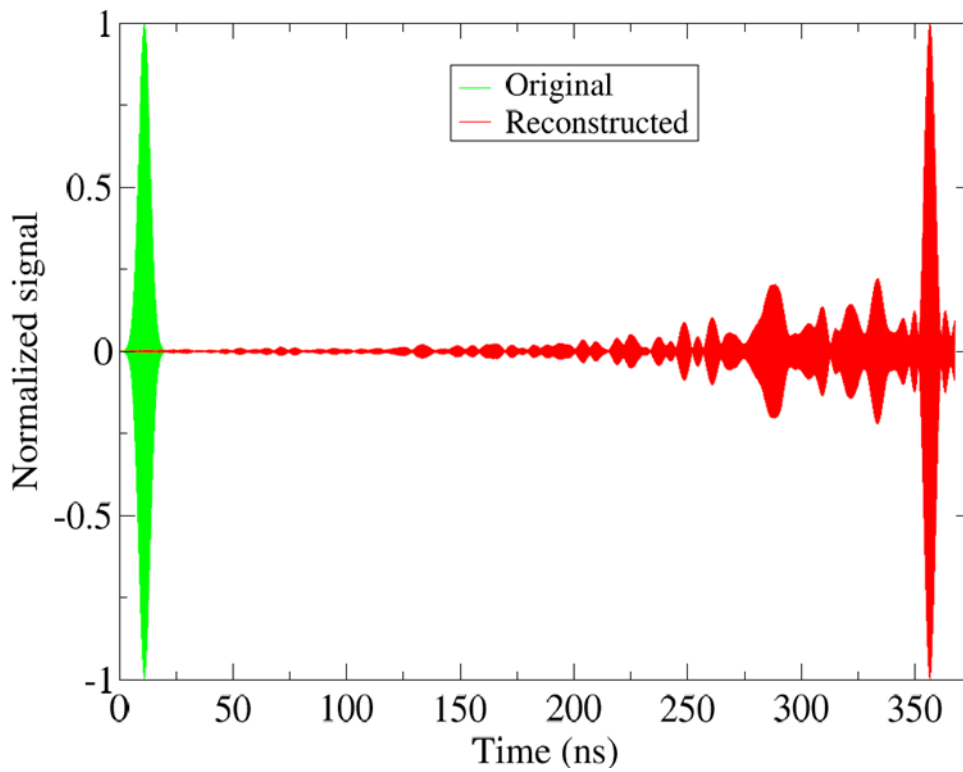


Figure 30 Original signal vs reconstructed signal (Simulation III).

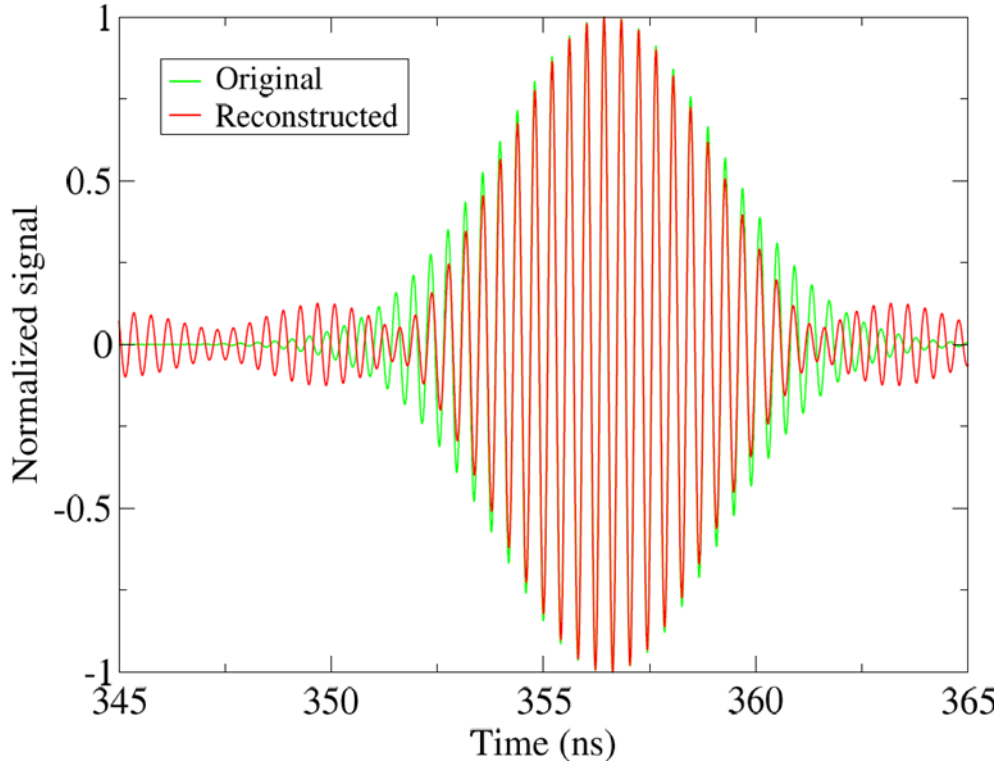


Figure 31 Original signal overlapped to the reconstructed signal (Simulation III).

Figure 32 reports the matching between the transmitted signal by the monopole and the received signal at the target point. Note that, as in Figure 29, the received signal is normalized to the maximum value assumed by the first gaussian envelope, which is related to the original signal that we want to reconstruct. The comparison between original and reconstructed signal is shown in Figure 33. Besides, Figure 34 illustrates the overlap between original and reconstructed signals. Adding the diffuser into the environment results in moderately better filtering out of side lobes at the expense of the reconstruction of the main beam, which slightly worsens. The time required to run Simulation IV is similar to that of Simulation III, thus there is no noticeable increase in the computational effort. After time reversal and reemission of the received signal computed by own-made FDTD code, we evaluate the spatio-temporal evolution of the module value of electric field,  $|E|$  (in V/m), in the working volume. It is done to verify the spatial focusing on the target point at the focusing time, related to the time in which there is the maximum value of the reconstructed signal.



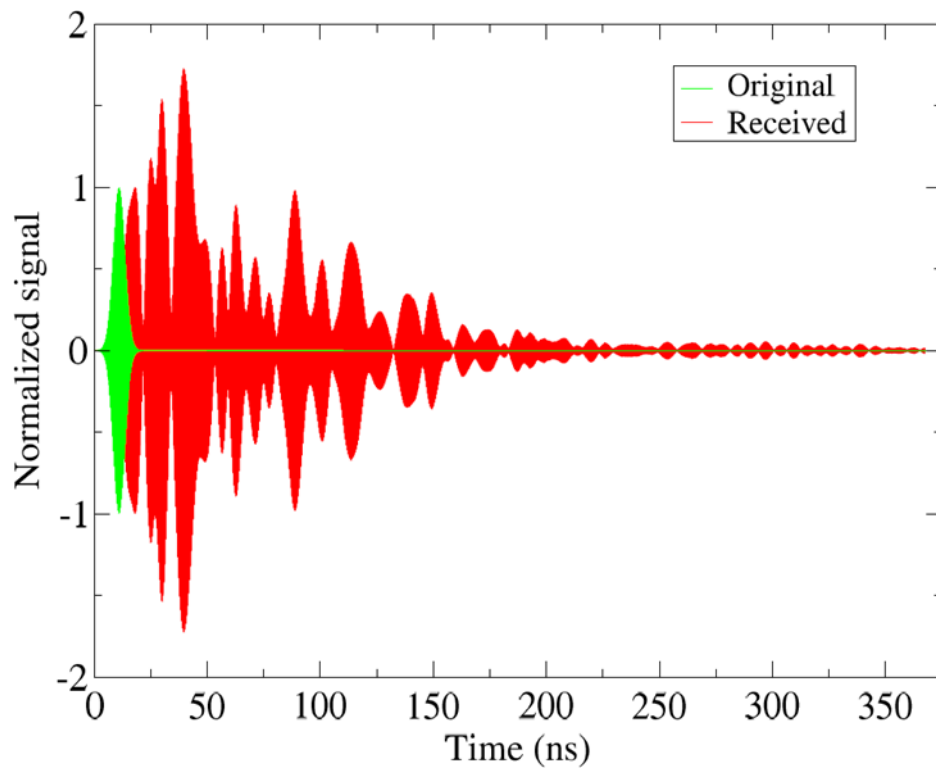


Figure 32 Original vs received signal (Simulation IV).

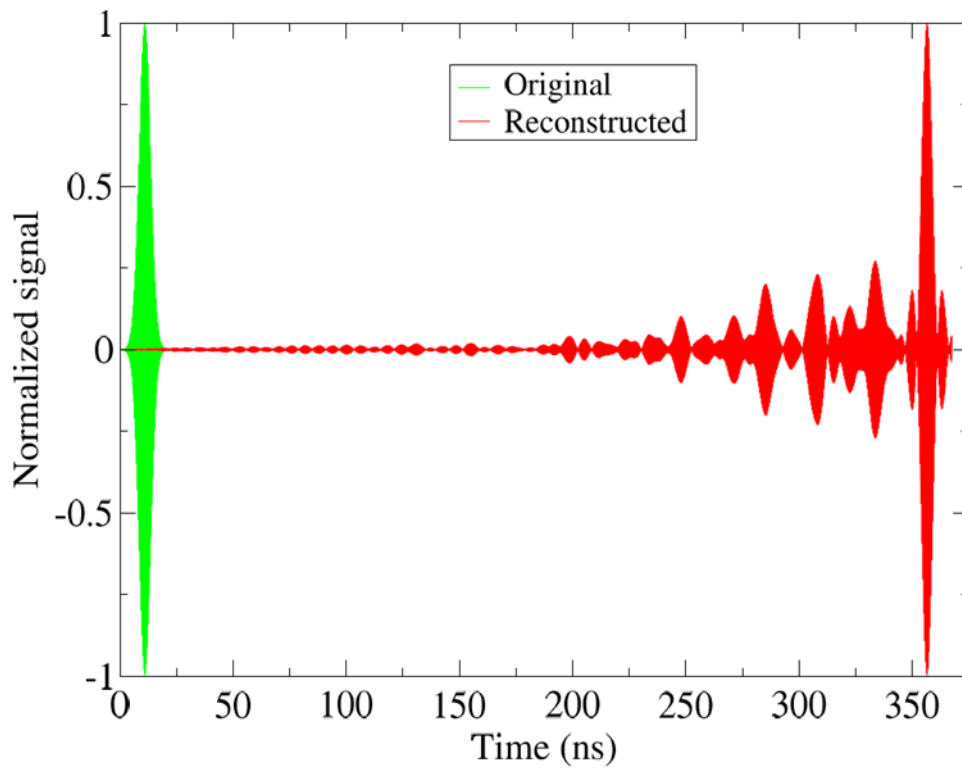


Figure 33 Original signal vs reconstructed signal (Simulation IV).

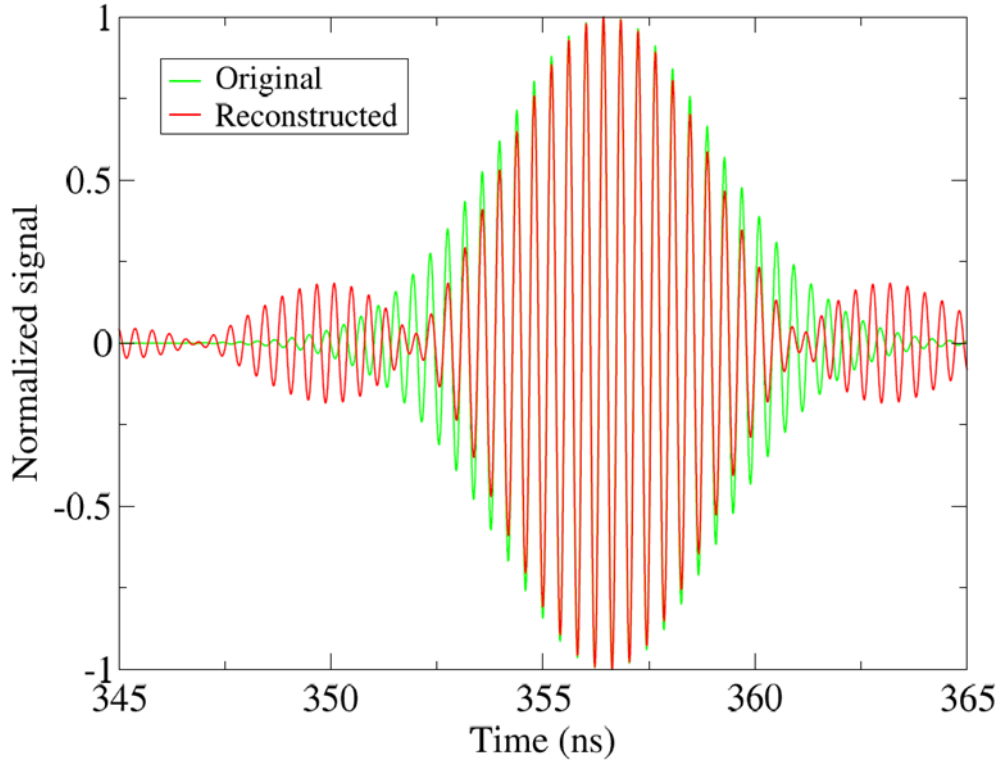


Figure 34 Original signal overlapped to the reconstructed signal (Simulation IV).

Referring to simulation IV, Figure 35 shows the contour plot of electromagnetic fields related to the transmission of the original input signal to the target point. We can point out an absence of electromagnetic fields focusing on the target point. The contour plot of electromagnetic field after the application of TR is shown in Figure 36, always concerning Simulation IV. A slight tendency of the electric fields to focus on the target point can be observed, which confirm the validity of the methodology in a short time. However, the most appreciable results in terms of spatial focusing concern Simulation I and II. Figure 37 and Figure 38 report the contour plots of electromagnetic fields regarding the transmission of original input signal. Also in these cases we do not have any electromagnetic field focusing on the target point. Instead, Figure 39 and Figure 40 display the contour plots of electromagnetic fields after the application of TR. Notice the improvements achieved by using a larger resonant chamber. According to obtained results, we state that the proposed methodology is an efficient method to focus on time domain the electromagnetic energy on human head.

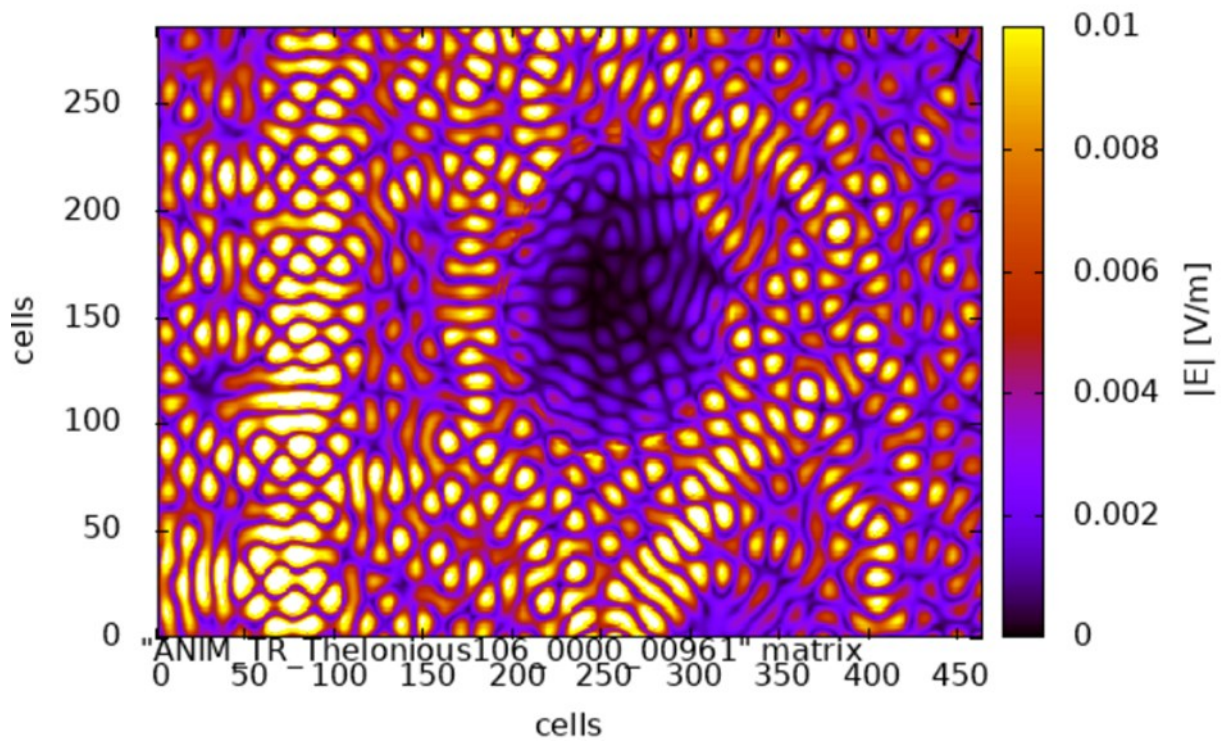


Figure 35 Contour plot of electromagnetic fields related to the transmission of the original input signal to the target point (Simulation IV).

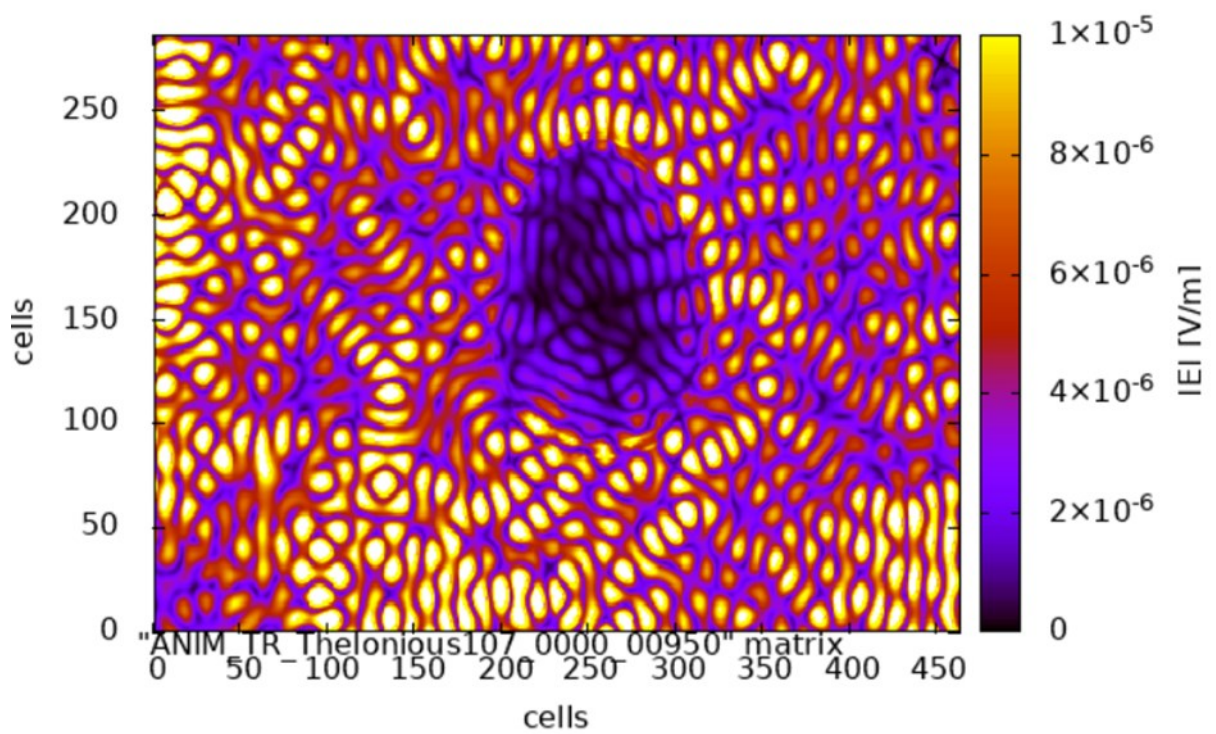


Figure 36 Contour plot of electromagnetic field after the application of TR (Simulation IV).

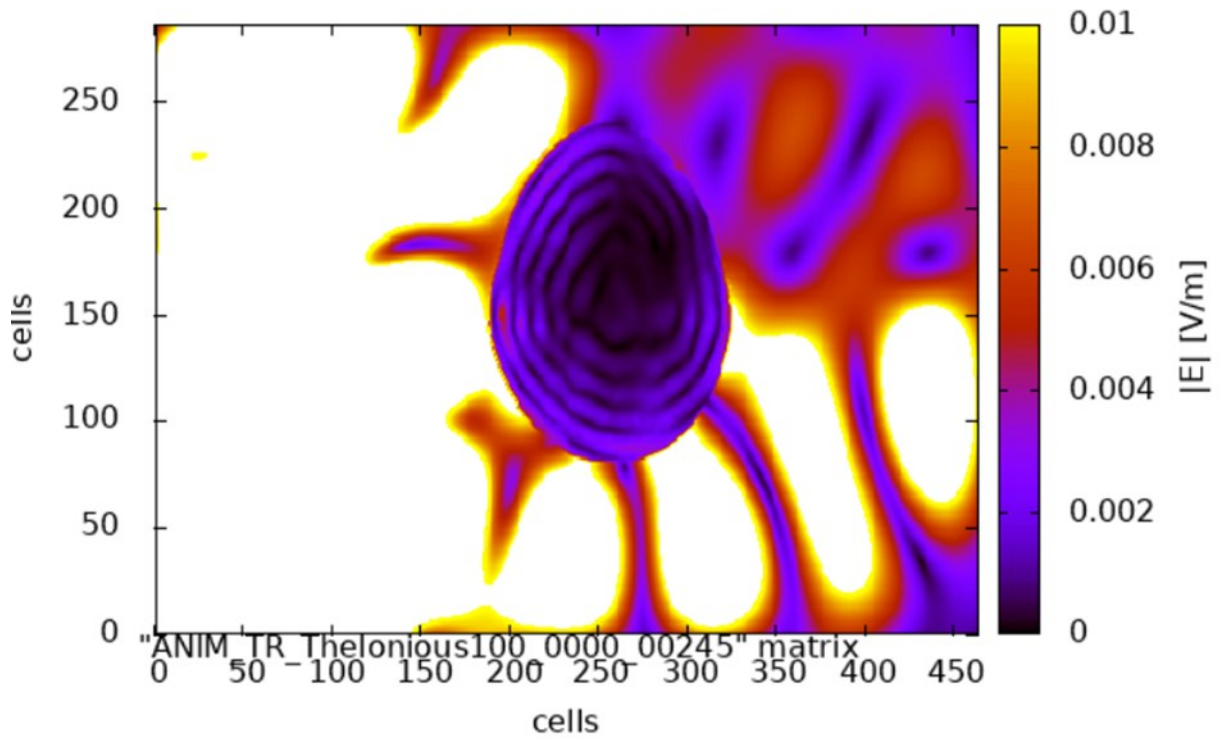


Figure 37 Contour plot of electromagnetic fields related to the transmission of the original input signal to the target point (Simulation I).

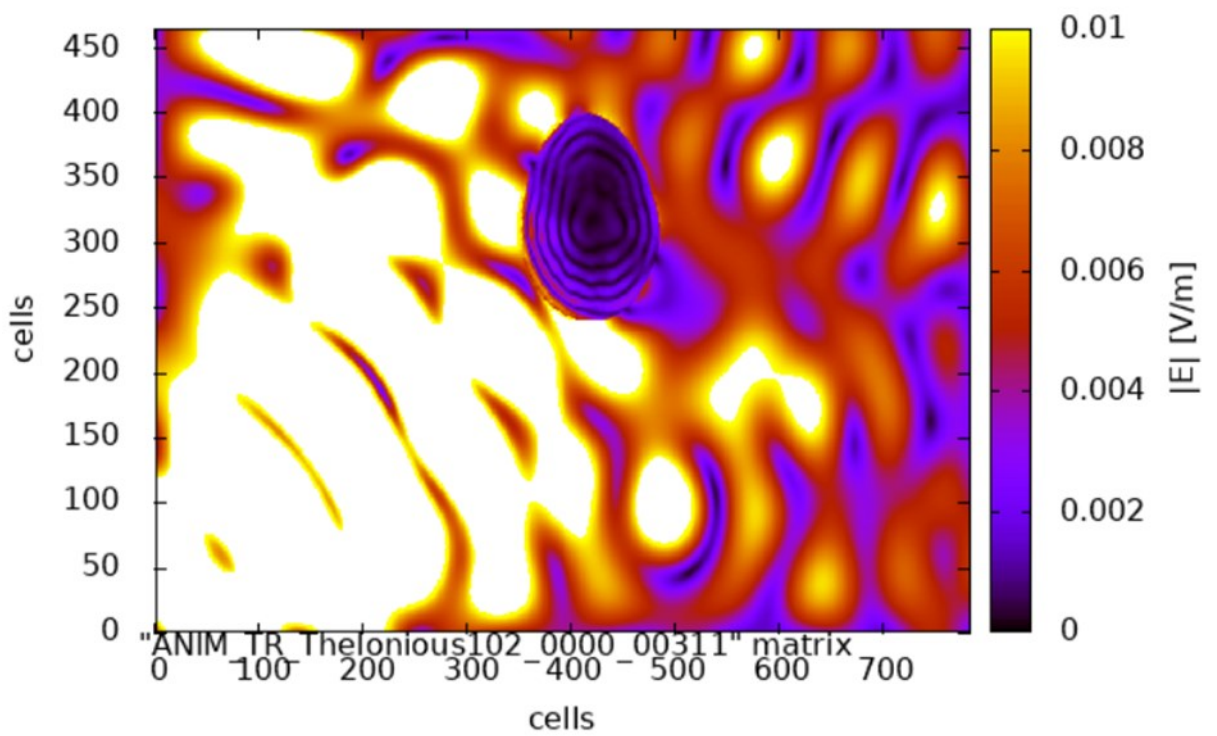


Figure 38 Contour plot of electromagnetic fields related to the transmission of the original input signal to the target point (Simulation II).

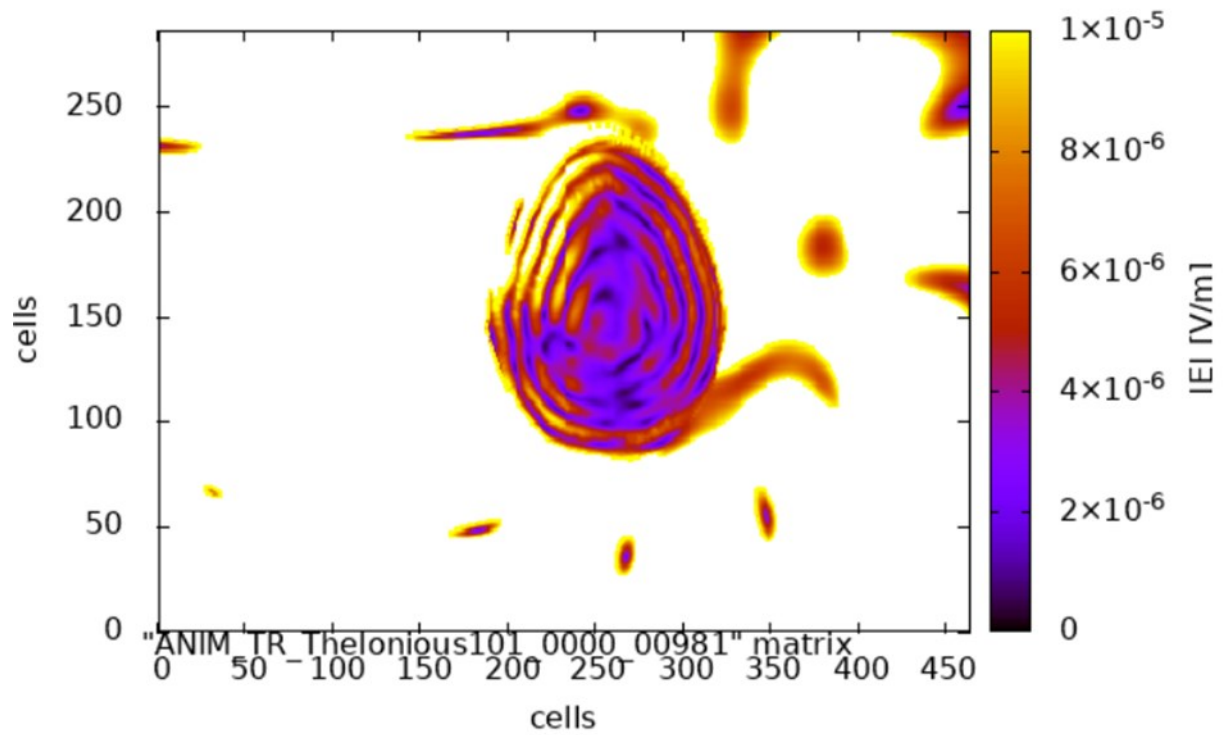
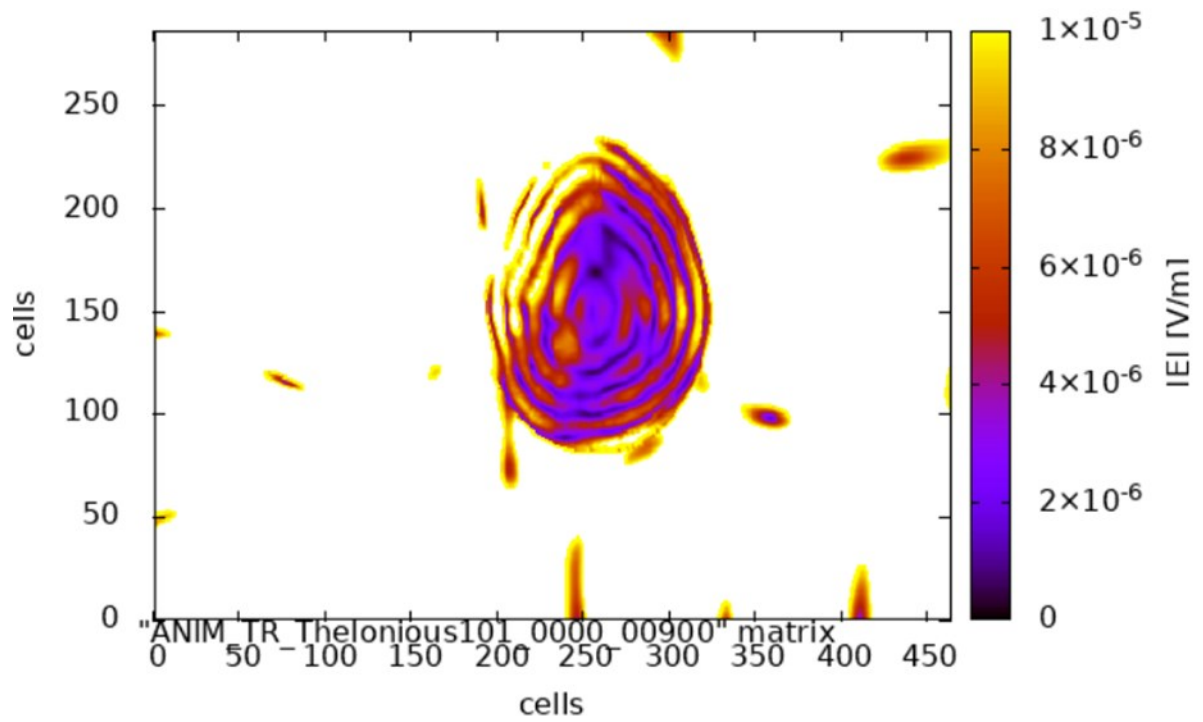


Figure 39 Contour plot of electromagnetic field after the application of TR (Simulation I). At the top there is a frame earlier than the one at the bottom.

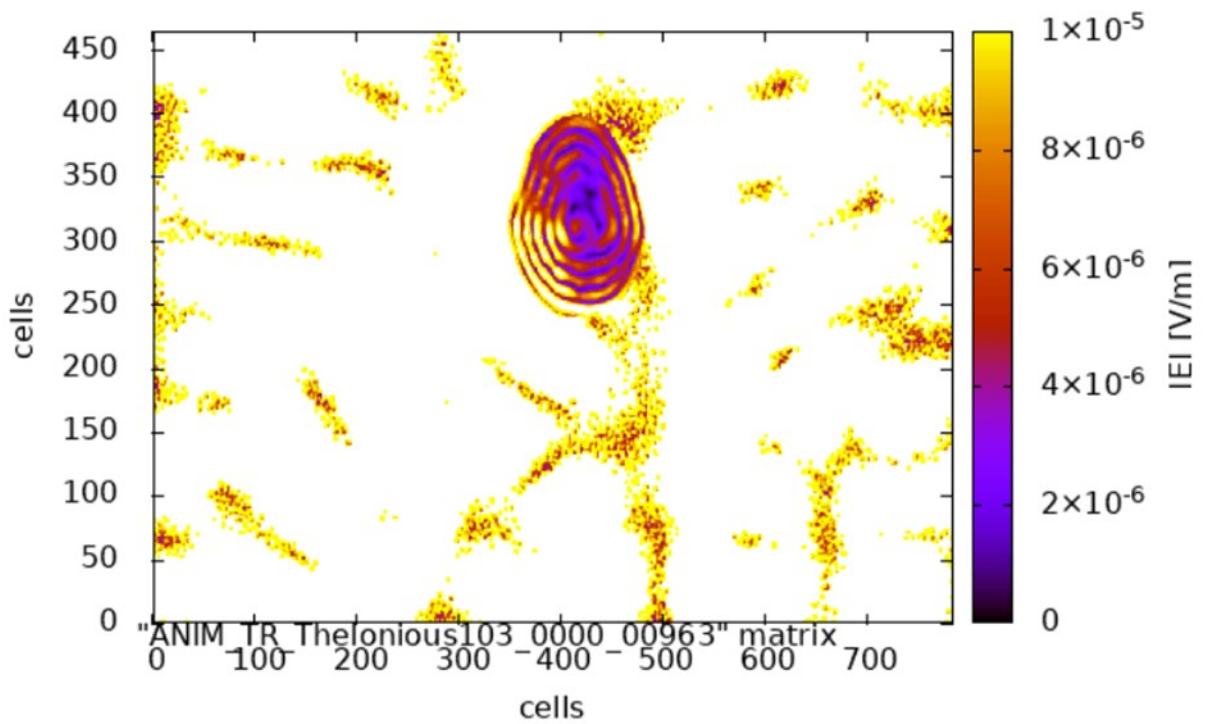
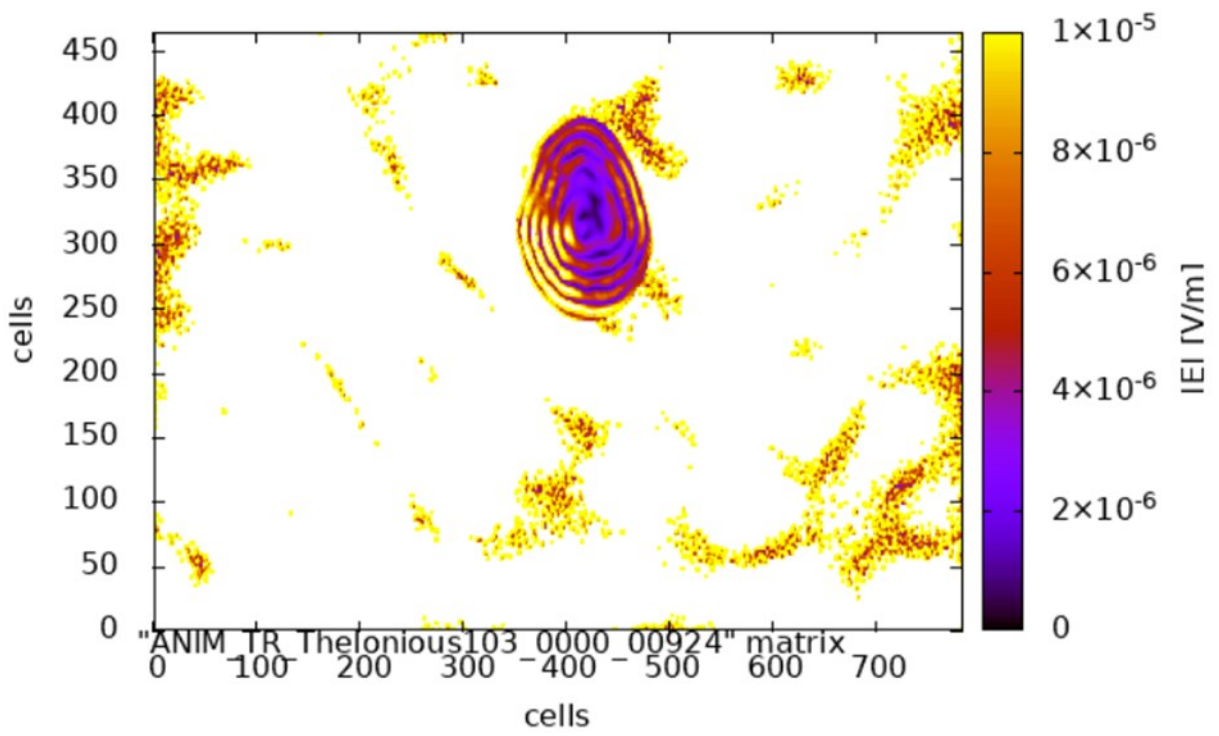


Figure 40 Contour plot of electromagnetic field after the application of TR (Simulation II). At the top there is a frame earlier than the one at the bottom.

## 5. Conclusions

We have proposed through this thesis a successful FDTD numerical approach of time reversal technique to focus, both spatially and temporally, electromagnetic energy on human head. From a practical point of view, it is simpler to carry out a parametric study numerically than experimentally. Indeed, a numerical study gives us the opportunity to be flexible in the choice of several technical configuration, i.e., the type and/or position of the antennas, the type and/or position of the diffuser, the design of the reverberation chamber, etc. Moreover, it helps in overcoming the ethical problems related to experimentation on living beings. The own-made FDTD code is relieved to be efficient in reaching its goal, but it requires to be run in high-performance computer due to the high computational effort. For exact TR focusing, Thelonious numerical model from the Virtual Family project is used because they constitute the gold standard for in silico biophysical modelling applications. The simulations are supposed to be performed into a reverberation chamber, which allows to exploit the several wave reflections on the metal walls, ensuring enough information to be recorded at target point. Furthermore, reverberation chamber allows to obtain a simplified absorption condition because if we finish the FDTD-simulation on a metal wall the tangential electric fields are zero. We have evinced that considering a medium with relative dielectric constant much higher than that of air, allows to significantly accelerate the simulation times and to maintain a good reconstruction of the original signal. Therefore, it represents a fair compromise between required computational effort and quality of original signal reconstruction, in order to fine-tune the methodology. Anyhow, a much finer spatial focusing is obtained considering air within the working environment and a larger reverberation chamber, which corresponds to an increase of the Q-factor and, in turn, of the number of wave modes. Limitations are mainly due to the ambitious choice of a very deep target point into the head, that make difficult the focusing of electromagnetic waves at a frequency of 2.45 GHz. Another constraint regards the reciprocity assumption.

It is easy to satisfy it in numerical simulations, but it needs a careful approach in the experimental applications. For simplicity, nothing should change between the forward and backward steps in order for TR to provide focusing. Thus, TR is difficult to be applied in systems where mechanical properties are time dependent, such as a change in wave speed due to global change in temperature. Anyway, TR exhibits several advantages, such as its efficiency in reverberation chamber, its applicability for system bounded in space and its capability to characterize complex structures. Future studies are recommended first to improve our numerical results, for example by considering a further larger reverberation chamber, taking into account the consequent increase of computational effort. Then, it would be interesting to experimentally confirm the numerical results, and so to proceed with experimental analysis. TR has emerged as a very interesting technique with potential applications in focusing and amplification of electromagnetic waves, biomedical engineering, imaging, EMC testing, wireless communication, etc. In medical contest, one may think of applying TR to both diagnostic and therapeutic fields. About diagnosis, the highly fine focusing of electromagnetic waves achieved by means of TR could be aimed at the design of devices able to optimize the interaction between electromagnetic fields and human tissues and to develop imaging approaches capable to characterize complex biological environments from the point of view of the electromagnetic properties. Concerning the therapeutic aspects, TR could be used to improve microwave hyperthermia methodologies, through the design and implementation of applicators capable of focusing the electromagnetic energy in the diseased tissue, while minimizing the side effects of the surrounding healthy tissue. Finally, it could be also used for the development of the so called 'theranostic' systems, which synchronously exploit both the diagnostic and therapeutic natures of microwaves, integrating a device for thermal therapy and another one to obtain information for the treatment design and to check work in progress's effectiveness.



## 6. Bibliography

- [1] A. Taflove and Susan C. Hagness, "Computational Electrodynamics: The FDTD Method (2nd Ed.)," no. June 2000, p. 439, 2000.
- [2] J. B. Schneider, "Understanding the Finite-Difference Time-Domain Method," 2021.
- [3] Richard Courant; Kurt Otto Friedrichs; Hans Lewy (1928). "Über die partiellen Differenzengleichungen der mathematischen Physik". *Mathematische Annalen* (in German). 100 (1): 32–74. Bibcode:1928MatAn.100...32C. doi:10.1007/BF01448839. JFM 54.0486.01. MR 1512478. S2CID 120760331.
- [4] J. VonNeumann and R. D. Richtmyer, "A method for the numerical calculation of hydrodynamic shocks," *J. Appl. Phys.*, vol. 21, no. 3, pp. 232–237, 1950, doi: 10.1063/1.1699639.
- [5] Yee, K.S., et al. (1966) Numerical Solution of Initial Boundary Value Problems Involving Maxwell's Equations in Isotropic Media. *IEEE Transactions on Antennas and Propagation*, 14, 302-307. <https://doi.org/10.1109/TAP.1966.1138693>.
- [6] A. Taflove, "Application of the FDTD Method to Sinusoidal Steady-State EM Problems," *Transaction on EMC*, vol. 22, no. 3. pp. 191–202, 1980.
- [7] A. Jimenez, "The Finite-Difference Time-Domain Method (FDTD)," *2-D Electromagn. Simul. Passiv. Microstrip Circuits*, no. 3, pp. 79–90, 2008, doi: 10.1201/9781420087062.ch4.
- [8] G. Mur, "Absorbing Boundary Conditions for the Finite-Difference Approximation of the Time-Domain Electromagnetic-Field Equations," *IEEE Trans. Electromagn. Compat.*, vol. EMC-23, no. 4, pp. 377–382, 1981, doi: 10.1109/TEMC.1981.303970.
- [9] J. P. Berenger, "A perfectly matched layer for the absorption of electromagnetic waves," *Journal of Computational Physics*, vol. 114, no. 2. pp. 185–200, 1994, doi: 10.1006/jcph.1994.1159.
- [10] K. Sankaran, "Are you using the right tools in computational electromagnetics?,"

- Eng. Reports*, vol. 1, no. 3, pp. 1–19, 2019, doi: 10.1002/eng2.12041.
- [11] M. Rafiee, S. Chandra, H. Ahmed, and S. J. McCormack, “Optimized 3d finite-difference-time-domain algorithm to model the plasmonic properties of metal nanoparticles with near-unity accuracy,” *Chemosensors*, vol. 9, no. 5, 2021, doi: 10.3390/chemosensors9050114.
- [12] B. E. Anderson, M. C. Remillieux, P. Y. Le Bas, and T. J. Ulrich, *Time reversal techniques*. 2018.
- [13] B. E. Anderson, M. Griffa, C. Larmat, T. J. Ulrich, and P. A. Johnson, “Time Reversal,” *Acoust. Today*, vol. 4, no. 1, p. 5, 2008, doi: 10.1121/1.2961165.
- [14] G. B. Lesovik, I. A. Sadovskyy, M. V. Suslov, A. V. Lebedev, and V. M. Vinokur, “Arrow of time and its reversal on the IBM quantum computer,” *Sci. Rep.*, vol. 9, no. 1, pp. 1–8, 2019, doi: 10.1038/s41598-019-40765-6.
- [15] F. Wu, J. L. Thomas, and M. Fink, “Time Reversal of Ultrasonic Fields – Part II: Experimental Results,” *IEEE Trans. Ultrason. Ferroelectr. Freq. Control*, vol. 39, no. 5, pp. 567–578, 1992, doi: 10.1109/58.156175.
- [16] G. Lerosey, J. De Rosny, A. Tourin, A. Derode, G. Montaldo, and M. Fink, “Time reversal of electromagnetic waves and telecommunication,” *Radio Sci.*, vol. 40, no. 6, pp. 1–10, 2005, doi: 10.1029/2004RS003193.
- [17] G. Lerosey, J. De Rosny, A. Tourin, A. Derode, and M. Fink, “Time reversal of wideband microwaves,” *Appl. Phys. Lett.*, vol. 88, no. 15, pp. 202–205, 2006, doi: 10.1063/1.2194009.
- [18] I. El Baba, S. Lallchre, and P. Bonnet, “Time Reversal for Electromagnetism: Applications in Electromagnetic Compatibility,” *Trends Electromagn. - From Fundam. to Appl.*, no. November 2015, 2012, doi: 10.5772/33739.
- [19] M. Fink, G. Montaldo, and M. Tanter, “Time-reversal acoustics in biomedical engineering,” *Annu. Rev. Biomed. Eng.*, vol. 5, pp. 465–497, 2003, doi: 10.1146/annurev.bioeng.5.040202.121630.
- [20] G. Lugrin, N. M. Parra, F. Rachidi, M. Rubinstein, and G. Diendorfer, “On the location of lightning discharges using time reversal of electromagnetic fields,” *IEEE Trans. Electromagn. Compat.*, vol. 56, no. 1, pp. 149–158, 2014, doi:

- 10.1109/TEMC.2013.2266932.
- [21] S. M. Anlage, J. Rodgers, S. Hemmady, J. Hart, T. M. Antonsen, and E. Ott, "New results in chaotic time-reversed electromagnetics: High frequency one-recording-channel time-reversal mirror," *Acta Phys. Pol. A*, vol. 112, no. 4, pp. 569–574, 2007, doi: 10.12693/APhysPolA.112.569.
- [22] S. M. Anlage, "Unique Applications of Time-Reversed Electromagnetic Waves," *2018 IEEE Symp. Electromagn. Compat. Signal Integr. Power Integrity, EMC, SI PI 2018*, pp. 1–126, 2018, doi: 10.1109/EMCSI.2018.8495195.
- [23] B. Xiao, T. M. Antonsen, E. Ott, and S. M. Anlage, "Focusing waves at arbitrary locations in a ray-chaotic enclosure using time-reversed synthetic sonas," *Phys. Rev. E*, vol. 93, no. 5, pp. 1–7, 2016, doi: 10.1103/PhysRevE.93.052205.
- [24] B. T. Taddese, G. Gradoni, F. Moglie, T. M. Antonsen, E. Ott, and S. M. Anlage, "Quantifying volume changing perturbations in a wave chaotic system," *New Journal of Physics*, vol. 15, no. 2, p. 023025, 2013.
- [25] M. Frazier, B. Taddese, T. Antonsen, and S. M. Anlage, "Nonlinear time reversal in a wave chaotic system," *Phys. Rev. Lett.*, vol. 110, p. 063902, Feb. 2013. [Online]. Available: <https://link.aps.org/doi/10.1103/PhysRevLett.110.063902>
- [26] B. T. Taddese, T. M. Antonsen, E. Ott, and S. M. Anlage, "The effects of non-uniform loss on time reversal mirrors," *AIP Advances*, vol. 4, no. 8, p. 087138, 2014. [Online]. Available: <https://doi.org/10.1063/1.4894448>
- [27] A. Cozza, "Statistics of the performance of time reversal in a lossy reverberating medium," *Phys. Rev. E*, vol. 80, p. 056604, Nov. 2009. [Online]. Available: <https://link.aps.org/doi/10.1103/PhysRevE.80.056604>
- [28] D. A. Hill, "electromagnetic theory of reverberation chamber.PDF," no. 1506, p. 58, 1998.
- [29] A. T. Frisco, L. Bastianelli, F. Moglie, and V. M. Primiani, "Time Reversal in Reverberation Chambers: Application to Lossy Media," *2019 IEEE Int. Symp. Electromagn. Compat. Signal Power Integrity, EMC+SIPI 2019*, pp. 664–669, 2019, doi: 10.1109/ISEMC.2019.8825289.
- [30] S. Grimnes & O.G. Martinsen; "Bioimpedance and Bioelectricity Basics". Elsevier;

- 2015.
- [31] S. Romanenko, R. Begley, A. R. Harvey, L. Hool, and V. P. Wallace, "The interaction between electromagnetic fields at megahertz, gigahertz and terahertz frequencies with cells, tissues and organisms: Risks and potential," *J. R. Soc. Interface*, vol. 14, no. 137, 2017, doi: 10.1098/rsif.2017.0585.
- [32] B. Li and B. J. Hu, "Imaging Method Based on Time Reversal Channel Compensation," *Int. J. Antennas Propag.*, vol. 2015, no. Mdm, 2015, doi: 10.1155/2015/894608.
- [33] L. Gun, D. Ning, and Z. Liang, "Effective Permittivity of Biological Tissue: Comparison of Theoretical Model and Experiment," *Math. Probl. Eng.*, vol. 2017, 2017, doi: 10.1155/2017/7249672.
- [34] R. Pethig, "Dielectric properties of body tissues," *Clin. Phys. Physiol. Meas.*, vol. 8, no. 4A, pp. 5-12, 1987, doi: 10.1088/0143-0815/8/4A/002.
- [35] K. S. Cole and R. H. Cole, "Dispersion and absorption in dielectrics I. Alternating current characteristics," *J. Chem. Phys.*, vol. 9, no. 4, pp. 341-351, 1941, doi: 10.1063/1.1750906.
- [36] C. Gabriel, S. Gabriel, and E. Corthout, "The dielectric properties of biological tissues: I. Literature survey," *Phys. Med. Biol.*, vol. 41, no. 11, pp. 2231-2249, 1996, doi: 10.1088/0031-9155/41/11/001.
- [37] S. Gabriel, R. W. Lau, and C. Gabriel, "The dielectric properties of biological tissues: \uppercase{II}. Measurements in the frequency range 10\uppercase{H}z to 20\uppercase{GH}z," *Phys. Med. Biol.*, vol. 41, no. 11, pp. 2251-2269, 1996.
- [38] A. Christ *et al.*, "The Virtual Family - Development of surface-based anatomical models of two adults and two children for dosimetric simulations," *Phys. Med. Biol.*, vol. 55, no. 2, 2010, doi: 10.1088/0031-9155/55/2/N01.
- [39] K. H. Awadalla and M. Maclean, "Monopole Antenna," no. 2, pp. 151-153, 1979.